

1

1 **Assessment of the Finite VolumE Sea Ice Ocean Model** 2 **(FESOM2.0), Part II: Partial bottom cells, embedded sea ice and** 3 **vertical mixing library [CVMix](#)~~CVMIX~~**

4
5 Patrick Scholz¹, Dmitry Sidorenko¹, Sergey Danilov^{1,2}, Qiang Wang¹, Nikolay Koldunov¹, Dmitry
6 Sein^{1,4}, Thomas Jung^{1,3}

7
8 ¹ Alfred Wegener Institute Helmholtz Center for Polar and Marine Research (AWI), Bremerhaven, Germany

9 ² Jacobs University Bremen, Department of Mathematics & Logistics, Bremen, Germany

10 ³ University of Bremen, Department of Physics and Electrical Engineering, Bremen, Germany

11 ⁴ Shirshov Institute of Oceanology, Russian Academy of Science, 36 Nahimovskiy Prospect, Moscow, Russia 117997

12
13 Correspondence to: Patrick Scholz (Patrick.Scholz@awi.de)

14 15 **Abstract**

16 The second part of the assessment and evaluation of the unstructured-mesh Finite-volumE Sea ice-Ocean
17 Model version 2.0 (FESOM2.0) is presented. It focuses on the performance of partial cells, embedded sea ice
18 and on the effect of mixing parameterisations available through the [CVMix](#)~~CVMIX~~ package.

19 It is shown that partial cells and embedded sea ice lead to significant improvements in the representation of
20 the Gulf Stream and North Atlantic Current as well as the circulation of the Arctic Ocean. In addition to the
21 already existing Pacanowski and Phillander (fesom_PP) and K-profile (fesom_KPP) parameterisations for
22 vertical mixing in FESOM2.0, we document the impact of several mixing parameterisations from the
23 Community Vertical Mixing ([CVMix](#)~~CVMIX~~) project library. Among them are the [CVMix](#)~~CVMIX~~ versions
24 of Pacanowski and Phillander (cvmix_PP) and K-profile (cvmix_KPP) parameterisations, the tidal mixing
25 parameterisation (cvmix_TIDAL), a vertical mixing parameterisation based on turbulent kinetic energy
26 (cvmix_TKE) as well as a combination of cvmix_TKE and the recent scheme for the computation of the
27 Internal Wave Dissipation, Energy and Mixing (IDEMIX). ~~The~~ IDEMIX parameterises the redistribution of
28 internal wave energy through wave propagation, nonlinear interactions and the associated imprint on the
29 vertical background diffusivity. Further, the benefit from using a parameterisation of [southern hemisphere](#)
30 sea ice melt season mixing in the surface layer (MOMIX) for reducing Southern Ocean hydrographic biases
31 in FESOM2.0 is presented. We document the implementation of different model components and illustrate
32 their behaviour. This paper serves primarily as a reference for FESOM users but is also useful to the broader
33 modelling community.

34 **1 Introduction**

35 Global unstructured-mesh ocean models start to be widely used in climate studies, including the recent
36 CMIP6 simulations (Semmler et al., 2020), although structured-mesh ocean general circulation models are
37 still more mature in terms of features, functionality and complexity due to their long development history.

2

38 However, step by step, also the unstructured-mesh ocean models acquire new features and catch up in their
 39 functionality. This paper continues the work by Scholz et al. (2019) in documenting the features available in
 40 Finite volume Sea ice Ocean Model version 2.0 (FESOM2.0, Danilov et al., 2017). It focuses on two
 41 aspects. The first ~~one~~ is about partial bottom cells and embedded sea ice, both of which essentially rely on
 42 the Arbitrary Lagrangian Eulerian (ALE) vertical coordinates used in FESOM2.0. The second ~~one~~ deals with
 43 mixing parameterizations enabled through the use of Community Ocean Vertical Mixing ([CVMix](#),
 44 [GriffiesCVMIX, Griffis](#) et al. 2015, Van Roekel et al. 2018) package.

45 Partial bottom cells were first introduced for a finite volume model by Adcroft et al., (1997), as an attempt to
 46 improve the representation of the bottom topography in general ocean circulation models. Adcroft et al.,
 47 (1997) introduces partial bottom cells as a compromise solution between the less accurate but
 48 computationally efficient full cell approach and the very accurate but computationally expensive shaved cell
 49 approach. Partial bottom cells are implemented in FESOM2.0 by using the vertical ALE approach of
 50 FESOM2.0 numerical core documented in Danilov et al. 2017.

51 Another feature made available through using ALE in FESOM2.0 is related to the sea ice-ocean interaction.
 52 Naturally, sea ice, more precisely the loading of sea ice, contributes to the ocean pressure. However in many
 53 ocean models, especially in the absence of surface mass fluxes or on fixed vertical grids, the loading is
 54 omitted and sea ice is treated as “levitating”. The option to consider sea ice loading is now implemented into
 55 FESOM2.0, which is called “embedded” sea ice and was first [mentioned by Hibler et al. \(1998\) and later](#)
 56 [further](#) introduced by [Hutchings et al. \(2005\) and](#) Campin et al. (2008). They state that the advection of sea
 57 ice in combination with the coupling of “embedded” sea ice through ice loading can be an important source
 58 of ocean variability especially in the vicinity of ice edges (Campin et al. 2008). The implementation of
 59 embedded sea ice relies on the zstar vertical-coordinate option in FESOM2 and also on the fact that [in the](#)
 60 [moment](#) the sea ice component is called on each time step of the ocean model.

61 Diapycnal mixing in the ocean is an essential process that acts on the ocean stratification and the distribution
 62 of heat, salt as well as passive tracers like nutrients, biological agents or CO₂. Various processes contributing
 63 to diapycnal mixing can act with different magnitudes over a wide range of horizontal and vertical scales,
 64 from several kilometers down to centimeters (Robertson and Dong, 2019). Due to the finite discretisation
 65 scale in all ocean models, the mixing processes can not be resolved and thus must be parameterized. The
 66 parameterisations of diapycnal mixing can be done in a variety of ways with different complexity, such as
 67 boundary layer schemes like the K-profile parameterisation of Large et al. (1994) or turbulent closure
 68 schemes like the one of Gaspar et al. 1990 and many others. A great innovation in the ocean modelling
 69 community is the development of software packages that contain a variety of vertical mixing
 70 parameterisations in a format that makes it easy to integrate them into existing model code (Fox Kemper et
 71 al. 2019). One of these software packages is the Community Ocean Vertical Mixing package ([CVMix](#),
 72 [GriffiesCVMIX, Griffis](#) et al. 2015, Van Roekel et al. 2018), which now also was integrated into FESOM2.0.
 73 [CVMixCVMIX](#) is tailored to be used in state of the art climate models to produce vertical profiles of

74 diffusivity and viscosity (Fox Kemper et al. 2019), providing a comparable mixing implementation over a
 75 wide spread of different ocean models such as MOM6, POP, MPAS and ICON. Such effort makes it easier
 76 to compare these models to each other. From the ~~CVMix~~~~CVMIX~~ package we implemented the Pacanowski
 77 and Philander 1981, the K-profile parameterization of Large et al. 1994 and the tidal mixing parameterisation
 78 of Simmons et al. 2004. Further, the infrastructure of the ~~CVMix~~~~CVMIX~~ library has been used to implement
 79 the turbulent kinetic energy (TKE) scheme of Gaspar et al. (1990) and the scheme for Internal Wave
 80 Dissipation and Mixing (IDEMIX) of Olbers and Eden (2013) in the same way as it is done in Gutjahr et al.
 81 (2020). It should be mentioned that neither TKE nor IDEMIX is yet part of the official ~~CVMix~~~~CVMIX~~
 82 package but will hopefully be added to the package in the future.

83 Beside the prime vertical mixing schemes, like the K-profile scheme, the Pacanowski and Phillander scheme
 84 and others that have the purpose to ~~create a general~~~~deliver a usable~~ mixing parameterisation for the entire
 85 ocean, and vertical mixing schemes like the tidal mixing scheme of Simmons et al. 2004 or IDEMIX that are
 86 used to parametrize internal wave processes which then result in a heterogeneous background diffusivity,
 87 there are also mixing parameterizations that aim at resolving regional processes. One of them was proposed
 88 by Timmerman and Beckmann (2004). It parameterises the wind driven mixing in the Southern Ocean
 89 especially when there is insufficient mixing during the melt seasons when other mixing schemes are used. It
 90 is used in FESOM2.0 to improve the otherwise too low stratification in the Southern Ocean and Weddell
 91 Sea.

92 The intention of this paper is to document the performance of the newly implemented features -- partial
 93 bottom cells, “embedded” sea ice, the vertical mixing parameterisations that come with the implementation
 94 of CMVIX and the local mixing parameterization of Timmerman and Beckmann (2004), based on comparing
 95 the associated hydrographic biases, changes in vertical convection and differences in Meridional Overturning
 96 Circulation, using a relatively coarse reference mesh.

97 The paper is structured as follows. First in Section 2 we describe the mesh configuration and model setup
 98 used in the simulations. The description and analysis of partial bottom cells, “embedded” sea ice and vertical
 99 mixing schemes is done in Section 3. A discussion and conclusion is given in Section 4.

100 **2 Model configurations**

101 We use ~~here~~ the FESOM2.0 coarse mesh configuration core2, which is the same mesh as in part 1. It consists
 102 of ~0.13M surface vertices, with a nominal resolution of 1° in the bulk of the ocean, ~25km north of 50°N ,
 103 $1/3^\circ$ in the equatorial belt and slightly enhanced resolution in the coastal regions. In the vertical, 48 unevenly
 104 distributed layers are used, with a vertical grid spacing stepwise increasing from 5m at the surface to 250 m
 105 towards the bottom.

106 All model simulations are initialised from the Polar Science Center Hydrographic winter Climatology
 107 (PHC3.0, updated from Steele et al., 2001) and forced by the CORE interannually varying atmospheric
 108 forcing fields (Large and Yeager, 2009) for the period 1948-2009. For each simulation a spin-up over three

109 full CORE cycles was applied, where each subsequent cycle was initialised with the final results from the
110 preceding cycle. All modelled data shown in this work are averaged over the period 1989-2009.

111

112 All model simulations except the one with the Turbulent-Kinetic-Energy (TKE) closure mixing of Gaspar et
113 al., 1990, use a non-constant latitude-dependent vertical background diffusivity with values between 10-4
114 m²/s and 10-6 m²/s, as described in Scholz et al., 2019. Further, all simulations use the Monin-Obukhov
115 length dependent vertical mixing parameterization of Timmermann and Beckmann, 2004 in the surface
116 boundary layer south of -50°S. The effects of this parameterisation on the simulated ocean state in
117 FESOM2.0 is described in section 3.4. The horizontal viscosity is computed via a modified harmonic Leith
118 approach (Fox-Kemper and Menemenlis, 2008) plus a biharmonic background viscosity (0.01 m²/s) . For
119 coarse-mesh setups, like the one used here, FESOM2.0 uses the Gent-McWilliams (GM) parameterisation
120 for eddy stirring (Gent et al., 1995; Gent and McWilliams, 1990) and we follow the implementation after
121 Ferrari et al., 2010. The isoneutral tracer diffusion (Redi, 1982) coefficient equals to that of GM, same as in
122 Scholz et al. (2019) and in previous FESOM versions (Wang et al. 2014). GM and Redi are scaled with
123 horizontal resolution with a maximum value of 3000 m²/s at 100 km horizontal resolution and change
124 linearly to zero between a resolution of 40 km and 30 km. In the vertical, they are scaled according to Ferrari
125 et al., 2010 and Wang et al., 2014. The simulations use as default the K-profile parameterisation for vertical
126 mixing (KPP, Large et al., 1994), a linear free surface (Scholz et al., 2019), levitating sea ice and a full
127 bottom cell approaches, unless otherwise stated.

128 **3 FESOM2.0 model components and evaluation**

129 **3.1 Partial bottom cells**

130 The concept of partial cells, as an attempt to improve the bottom representation in general ocean circulation
131 models, ~~which~~ was first introduced for the finite volume approach by Adcroft et al., (1997). Although an
132 early version of partial cells was developed by Cox, (1977), and used by Semtner and Mintz, (1977) and
133 Maier-Reimer et al., (1993), it has never got officially released (Griffies et al., 2000). Adcroft et al.
134 (1997) presented three different cases. The first one is the conventional full cell approach, where the depth of
135 the ocean bottom is approximated with the nearest standard depth level of the vertical model discretization.
136 The second one is the partial cell approach in which the bottom level can take any intermediate depth within
137 the cell, thus capturing water columns more accurately. In these two cases, the bottom features a “stepped”
138 topography and the jump of the steps is smaller for the partial cell approach (Adcroft et al., 1997). The third
139 case introduced by Adcroft et al., (1997) is a shaved cell approach, which assumes a constant slope within
140 each bottom cell and gives the best approximation for a continuous bottom topography. Adcroft et al.
141 (1997) showed that the shaved cell approach gives the most accurate results, but induces a significant
142 increase in computational demand, whereas the partial cell approach is a good compromise between the low

143 computational demand of the full cell approach and the increased accuracy of the shaved cell approach.
 144 Hence, most ocean models (e.g. NEMO, MOM6, MPAS, POP) including FESOM2.0 went in favor of the
 145 partial cell approach.

146 For the implementation of partial cells in FESOM2.0 we follow the work of Pacanowski and Gnanadesikan,
 147 (1998), which implemented partial cells for the B-grid discretization in MOM2 with efforts to minimize
 148 pressure gradient errors and spurious diapycnal mixing. They addressed that calculating horizontal pressure
 149 gradients needs some special attention for partial cells since not all grid points within the bottom layer are at
 150 the same depth. In FESOM2.0, we compute pressure gradient force based on the density Jacobian approach
 151 as used by Shchepetkin, (2003) and not the pressure Jacobian approach proposed by Pacanowski and
 152 Gnanadesikan, (1998). The density Jacobian approach is less prone to pressure-gradient error than using
 153 pressure Jacobian, and therefore the model is more stable. Furthermore, we limited the thickness of the
 154 partial bottom cell to be at least half of the full cell layer thickness to reduce the possibility of violating the
 155 vertical Courant–Friedrichs–Lewy (CFL) criterion.

156 Using a B-grid like discretisation, where the scalars are located at vertices of a triangular mesh while the
 157 velocities are located at the centroids of the triangular elements, makes it necessary to define the partial cells
 158 at both locations. First, the partial bottom depth is defined at the centroids of the triangular elements based
 159 on the real bottom topography considering the aforementioned limitation. Then, the ~~vertex~~ ~~vertice~~ partial
 160 bottom depth is derived from the deepest partial bottom of the surrounding triangular elements (see
 161 schematic representation in Suppl. 1).

162 In order to demonstrate the effect of the partial cells on the simulated ocean state we performed two model
 163 simulations using the full cell and partial cell approaches, respectively. We investigate, first, the temperature
 164 biases of the full cell approach with respect to the data of the World Ocean Atlas 2018 (WOA18, Locarnini
 165 et al., 2018; Zweng et al., 2018, in the left column of Fig. 1) and, second, the temperature differences
 166 between partial cell and full cell (partial-full) averaged over five different depth ranges 0-250m, 250-500m,
 167 500-1000m, 1000-2000m and 2000-4000m (in the right column of Fig. 1).

168 The full cell setup (Fig. 1, left) shows positive climatological temperature ~~bias in~~ ~~basin~~ the northern and
 169 southern Pacific, the Atlantic equatorial ocean as well as in the central Indian Ocean through the depth
 170 ranges of 0-250m, 250-500m and 500-1000m. In the same depth ranges there are also negative biases in the
 171 North Atlantic (NA) subtropical gyre and in the equatorial and southern subtropical Pacific. The depth
 172 ranges of 250-500m and 500-1000m indicate cold biases in the Southern Ocean (SO) and around the coast of
 173 Antarctica. The deeper depth ranges (1000-2000m and 2000-4000m.) indicate small negative temperature
 174 biases in most of the world oceans, except for the Atlantic and Arctic Ocean (AO), which possess a small
 175 warming bias in the depth ranges. The Arctic warming anomaly at these depths originates largely from a
 176 vertically too much extended Atlantic water inflow branch (not shown), which is a typical feature of coarse
 177 resolution models (e.g., Ilicak et al. 2016 ~~Hieak2016~~).

178 Using partial cells (Fig. 1, right) leads to profound changes especially at the position of zonal fronts in the

179 North and South Atlantic. In the depth ranges of 0-250 m, 250-500 m and 500-1000 m in the NA, partial
 180 cells lead to a cooling in the Labrador Sea (LS) and Irminger Sea (IS) as well as along the path of the Gulf
 181 Stream (GS) and North Atlantic Current (NAC), except for the area around -30°W , 50°N which is
 182 characterised by warming. In the upper South Atlantic (SA), partial cells lead to a northward shift of Brazil–
 183 Malvinas Confluence Zone expressed by a dipole of warmer South Atlantic Current (SAC) and cooler
 184 Antarctic Circumpolar Current (ACC). Further, partial cells lead to a predominant cooling in the SO Atlantic
 185 sector and parts of the Indian Ocean sector, while the Pacific sector of the SO and most of the Antarctic
 186 coastal areas are dominated mostly by warming anomalies. The Arctic Ocean features a slight warming
 187 anomaly at all depths, except for the surface, when using partial cells instead of full cells. [The table in Suppl.](#)
 188 [2 shows the regional \(\$-80^{\circ}\text{W} < \text{lon} < 5^{\circ}\text{E}\$, \$35^{\circ}\text{N} < \text{lat} < 70^{\circ}\text{N}\$ \) temperature standard deviation and root mean](#)
 189 [square error with respect to WOA18, with and without partial cells. It proves that partial cell lead to a](#)
 190 [significant improvement especially in the upper and intermediate ocean depth range, while the biases in the](#)
 191 [very deep ocean marginally increase.](#)

192 Fig. 2 shows the same as Fig. 1 but for salinity. Here, with respect to WOA18, the full cell run indicates a
 193 generally fresher AO for the surface- and the 250-500 m depth range. Further negative salinity biases can be
 194 found within the upper three depth ranges in the equatorial Pacific, north and south subtropical Atlantic, at
 195 the position of the Atlantic northwest corner, northern IO as well as parts of the SO. Strong positive salinity
 196 biases with full cells can be found in the surface depth range of the North Pacific and in the Chukchi- and
 197 Beaufort Sea. Further positive salinity biases in the 250-500 m and 500-1000 m depth ranges are found along
 198 the pathway of the Gulf Stream as well as in the equatorial Atlantic and central IO. The deep depth range of
 199 1000-2000m has positive salinity anomalies in the Northern and Southern Atlantic and negative salinity
 200 biases in the Mediterranean outflow branch and IO.

201 Using partial cells leads to an increase in salinity throughout all depth ranges of the AO relative to using full
 202 cells. Further, a salinity increase at the position of the “cold blob”, in the GIN sea, in the eastern South
 203 Atlantic and parts of the SO can be observed within the upper three depth ranges. Compared to full cells,
 204 using partial cells reduces salinity along the pathway of the GS, the Antarctic Circumpolar Current (ACC) in
 205 the South Atlantic and along the coast of Antarctica.

206 The differences in the horizontal velocity speed between partial and full cells (Fig. 3), for the depth ranges of
 207 0-250 m, 250-500 m, 500-1000 m, 1000-2000 m, 2000-4000 m and at the bottom, reveal that with partial
 208 cells the velocity in the East Greenland Current (EGC), West Greenland Current (WGC) and Labrador
 209 Current (LC) are stronger by up to 0.02 m/s through all depth ranges presented here. The upper differences
 210 reveal that partial cells lead to a weakening and a slight southwards shift of the NAC between -45°W and -
 211 30°W , and a more pronounced tendency towards a northwest bend of the NAC between -30°W and -15°W ,
 212 which is nevertheless still too far eastward. By using partial cells the pathway of the Irminger Current (IC)
 213 moves closer to the continental slope.

214 [In terms of absolute northern and southern hemispheric maximum mixed layer depth \(MLD\), using full cell](#)

215 (Fig. 4a and 4b), FESOM2.0 features known intensive convection in the Labrador Sea and Irminger Sea,
 216 northern Greenland Sea as well as central Weddell Sea (Marshall and Schott 1999, Sallée et al. 2013,
 217 Danabasoglu et al. 2014).

218 ~~In terms of absolute and anomalous northern and southern hemispheric maximum mixed layer depth (MLD),~~
 219 ~~using partial cells leads to a slight MLD decrease in the southern LS, IS and northern Greenland-Iceland-~~
 220 ~~Norwegian (GIN) Seas, and a slight MLD increase along the pathway of the IC and in the southern and~~
 221 ~~central GIN Seas (Fig. 4c). In the southern hemisphere, partial cells have a more pronounced effect, leading~~
 222 ~~to a significant, up to 1000 m, decrease in MLD in the central Weddell Sea (WS) and a minor increase in~~
 223 ~~MLD of around 300 m along the eastern continental slope of the Antarctic Peninsula.~~

224 The anomalous northern and southern hemispheric maximum mixed layer depth (MLD), using partial cells
 225 features a slight MLD decrease in the southern LS, IS and northern Greenland-Iceland-Norwegian (GIN)
 226 Seas, and a slight MLD increase along the pathway of the IC and in the southern and central GIN Seas (Fig.
 227 4c). In the southern hemisphere, partial cells have a more pronounced effect, leading to a significant, up to
 228 1000 m, decrease in MLD in the central Weddell Sea (WS) and a minor increase in MLD of around 300 m
 229 along the eastern continental slope of the Antarctic Peninsula.

230 The differences between using full cells and partial cells in Global-, Atlantic- and Indo-Pacific Overturning
 231 Circulation (Fig. 5) are rather small with magnitudes of less than 1Sv. Both cases feature an upper AMOC
 232 circulation cell of ~16 Sv and an Antarctic Bottom Water (AABW) cell with strength between -1 Sv and -2
 233 Sv. One can summarize that partial cells lead to ~~an a-clear~~ improvement of the circulation pattern, especially
 234 regarding the ~~reduced zonality~~ branch of the Gulf Stream and NAC branch even in rather coarse resolved
 235 configurations.

236 **3.2 Embedded sea ice**

237 As described in Scholz et al. (2019), FESOM2.0 supports the full free surface formulation with two possible
 238 options, zlevel and zstar (Adcroft and Campin, 2004). Both options allow for surface freshwater exchanges
 239 which can modify the thickness of the surface layer and thus decrease or increase salinity in the surface
 240 layer. This avoids the need of virtual salinity fluxes, which are required in the linear free surface (linfs)
 241 approach when the layer thicknesses are kept fixed. Using virtual salinity fluxes has the potential to affect
 242 the model integrity on long timescales and change local salinities with certain biases (Scholz et al., 2019).

243 In reality part of sea ice is embedded in the ocean with impact on the ocean pressure below. In the model,
 244 when the sea ice loading is omitted, the “levitating” sea ice (Campin et al., 2008) does not impose pressure
 245 on the ocean. This is the default case in the case of linfs but also applicable to zlevel and zstar. The other
 246 case when ice-loading is considered has “embedded” sea ice (Rousset et al., 2015), which depresses the sea
 247 surface according to its mass. Since it affects the layer thicknesses, this case is only available for the full free
 248 surface cases of zlevel and zstar. Although freezing and melting have no direct effect on the oceanic
 249 pressure, the divergence of the ice transport does modify the ice-loading fields and influences the hydrostatic

250 pressure (Campin et al., 2008). As mentioned by Campin et al., 2008, this effect could be compensated by
 251 the divergence of the oceanic transport in the special case where sea ice and ocean velocities match, but in
 252 reality sea ice and ocean velocities are ~~not~~~~rarely~~ identical especially in the presence of high frequency wind
 253 forcing. Therefore, sea ice dynamics in combination with the ice-loading coupling can be a source of oceanic
 254 variability especially near the ice-edge where ice divergence/convergence is large (Campin et al., 2008).
 255 However, using embedded sea ice harbours the risk that the amount of sea ice loading due to excessive
 256 accumulation and the resulting depression in the surface elevation may result in a depletion of the surface
 257 layer thickness, when the zlevel option is used, where only the surface layer is allowed to change. To avoid
 258 this issue, we limit in FESOM2.0 the maximum ice loading to a sea ice height of 5m when the zlevel option
 259 is used. In case of using zstar, the problem is less severe, since here the change in elevation is distributed
 260 over all vertical layers, except for the bottom one. This makes zstar to be the recommended option when
 261 using embedded sea ice, as also stated by Campin et al., 2008.

262 To show the effect of embedded sea ice on the simulated ocean state, two simulations were carried out using
 263 the zstar option of FESOM2.0, one with levitating (omitting the effect of sea ice loading on ocean pressure)
 264 the other with embedded sea ice (including the effect of sea ice loading on ocean pressure).

265 Fig. 6 shows the sea ice concentration (SIC) for March and September in the levitating sea ice case and the
 266 difference between the embedded and levitating sea ice cases. Superimposed are the simulated (solid) and
 267 observed (dashed, Cavalieri et al., 1996) contour line of the 15% sea ice extent. The northern hemispheric
 268 March sea ice edge (Fig. 6a) shows a good agreement with observational data for the LS, IS and Bering Sea
 269 but reveals a too far southwards extension in the Greenland Sea and Barents Sea. The simulated northern
 270 hemispheric ~~(September)~~~~September~~ sea ice extent (Fig. 6b) is larger than the observations. The southern
 271 hemispheric ~~(March)~~~~March~~ sea ice extent is underestimated in the simulation, while the simulated southern
 272 hemispheric ~~(September)~~~~September~~ sea ice extent is in good agreement with the observation.

273 Using the embedded sea ice leads to an increase in the SIC in the Greenland Sea by around 6% in March. In
 274 September, embedded sea ice leads to positive SIC anomalies in the eastern- and negative anomalies in the
 275 western AO. In the southern hemisphere, embedded sea ice leads to a heterogeneous pattern of small positive
 276 and negative changes along the sea ice edge. The corresponding results for the sea ice thickness are shown in
 277 Suppl. 4, here both March and September northern hemisphere sea ice thickness anomalies reveal a dipole
 278 like pattern with reduced sea ice thickness in the area of the Beaufort gyre and increased sea ice thickness in
 279 the easter AO and region of the transpolar drift when using embedded sea ice.

280 Regarding the changes in the ocean, Fig. 7 shows the temperature (left column) and salinity (right column)
 281 differences between the embedded and levitating (embedded minus levitating) sea ice cases averaged over
 282 the depth ranges 0-250 m, 250-500 m, 500-1000 m, 1000-2000 m and 2000-4000 m. The temperature and
 283 salinity differences reveal that a significant warming of up to 0.5°C and a salinification of up to 0.10 psu
 284 occurs in almost the entire AO due to embedded sea ice, except in a thin stripe along the eastern continental
 285 shelf of the AO that shows negative anomalies in the depth ranges of 0-250 m, 250-500 m and 500-1000 m.

286 The changes in temperature and salinity can be explained by the changes in ocean currents. Figure 8 depicts
 287 the speed of the horizontal currents in levitating (1st column) and embedded (2nd column) sea ice cases as
 288 well as their difference (3rd column). Using embedded sea ice leads to an increase in the speed along the
 289 entire boundary current of the Eurasian Basin and along the Lomonosov Ridge, that can be found in all three
 290 presented depth ranges. The increase in the velocity of the boundary currents, caused by using embedded sea
 291 ice, leads to an enhanced heat and salt transport in the Atlantic water layer originating from the Fram Strait,
 292 which results in a warmer and more saline intermediate depth in the Arctic Ocean. The increase in
 293 temperature and salinity, especially in the surface layers of the AO using embedded sea ice reduces existing
 294 local biases (see Fig. 1 and Fig. 2) that occur when using levitating sea ice. On the whole it can be stated that
 295 using embedded sea ice instead of levitating sea ice has some significant effect on the ocean dynamics of the
 296 AO, but no effect in the Southern Ocean or Antarctic marginal seas.

297 **3.3 Implementation and evaluation of vertical mixing schemes**

298 Besides the already existing Pacanowski and Philander (fesom_PP, Pacanowski and Philander, 1981) and
 299 ~~MOM4~~~~MOM5~~ K-profile (fesom_KPP, Large et al., 1994) vertical mixing parameterizations in FESOM2.0
 300 that were based on the implementation in the predecessor version FESOM1.4, the vertical mixing
 301 parameterizations of the Community Vertical Mixing (~~CVMix~~~~CVMIX~~, Griffies et al., 2015) project have
 302 been now added as well. This includes the ~~CVMix~~~~CVMIX~~ vertical mixing of: Pacanowski and Philander
 303 (cvmix_PP), the [POP \(Parallel Ocean Program\) ~~MOM6~~](#)-K-profile (cvmix_KPP) parameterization, the tidal
 304 mixing parameterization of Simmons et al., (2004) (cvmix_TIDAL) and the turbulent kinetic energy
 305 (cvmix_TKE) mixing of (Gaspar et al., 1990) in combination with the Internal Wave Dissipation, Energy
 306 and Mixing (IDEMIX) parameterization (Olbers and Eden, 2013 and Eden and Olbers, 2014) . Although
 307 cvmix_TKE and IDEMIX are not yet a part of the ~~CVMix~~~~CVMIX~~ project, they use its libraries in the
 308 background and will join the project in the future. ~~CVMix~~~~CVMIX~~ is used by a variety of models, such as
 309 MOM6, POP, MPAS or ICON and provides an opportunity of a cross model-spanning vertical mixing
 310 implementation that allows for an enhanced cross-model intercomparison.

311

312 **3.3.1 Comparison of cvmix_KPP, cvmix_PP with previous fesom_KPP and fesom_PP** 313 **implementation**

314 In FESOM2.0 we implemented cvmix_PP and cvmix_KPP in addition to its previous implementations
 315 fesom_PP and fesom_KPP that were adopted from FESOM1.4. The difference between cvmix_PP and
 316 fesom_PP lies in the background coefficient for viscosity which is considered in cvmix_PP but not in
 317 fesom_PP when computing the diffusivity, following the experience with FESOM1.4 which did not need to
 318 be more diffusive. The difference between cvmix_KPP and fesom_KPP lies mainly in the treatment of the
 319 squared velocity shear and buoyancy difference with respect to the surface, [although CVMix does not make](#)
 320 [any specific requirements here](#). In cvmix_KPP [we synchronized the implementation with our project partner](#)

321 ~~models MPIOM and ICON-o and compute the cvmix_KPP surface quantities~~ the surface quantities are
 322 ~~computed~~ by averaging over 10% of the boundary layer depth as recommended by the Monin-Obukov
 323 ~~surface layer~~ (Griffies et al. 2015) while in fesom_KPP the surface values are linked to the first layer in the
 324 model which was inspired by the implementation in the older MOM4.

325 Suppl. 52 displays the temperature (1st and 2nd column) and salinity (3rd and 4th column) biases of fesom_KPP
 326 with respect to WOA18 (1st and 3rd column) as well as the difference between fesom_PP and fesom_KPP (2nd
 327 and 4th column). In the surface depth range the climatological temperature and salinity biases of fesom_KPP
 328 with respect to WOA18 are largely negative in the tropical and subtropical Pacific, North and South Atlantic
 329 as well as AO, and positive in tropical Atlantic and Indian Ocean, Southern Ocean, Labrador Sea, GIN Seas
 330 and the marginal seas of the North Pacific. The subsurface depth ranges of 250-500 m and 500-1000 m are
 331 dominated by largely positive temperature biases, except for the Southern Ocean, the pathway of the GS and
 332 NAC and the northern Indian Ocean. The salinity biases in the 250-500 m and 500-1000 m depth range
 333 preserve largely the pattern from the surface layer except for an increasing and expanding positive salinity
 334 bias in the tropical Atlantic, reduced positive salinity biases in the Indian Ocean and northern Pacific as well
 335 as reduced negative biases in the Arctic Ocean. The 1000-2000 m depth range features small warm biases in
 336 the AO and GIN seas, positive temperature and salinity biases in the LS and the South Atlantic, negative
 337 temperature and salinity biases in the eastern North Atlantic (possibly due to weak mediterranean outflow)
 338 and small negative temperature and salinity biases in the Pacific and Indian Ocean. The very deep depth
 339 range of 2000-4000 m reveals rather small warming bias for the entire Atlantic and SO.

340 ~~fesom~~Fesom_KPP and fesom_PP produced rather small temperature and salinity differences (note different
 341 colorbar ranges between 1st & 2nd and 3rd & 4th column), considering the biases with respect to the WOA18
 342 climatology. Employing fesom_PP has the tendency to be slightly warmer almost everywhere in the
 343 subsurface layers and slightly saltier especially in the AO and fresher in the surface layer of the subtropical
 344 and equatorial ocean compared to using fesom_KPP. Looking at the maximum MLD between fesom_PP and
 345 fesom_KPP (Suppl. 6) it can be seen that fesom_PP has the tendency to produce an up to 500m shallower
 346 deep convection in LS and WS when compared to fesom_KPP.

347 Fig. 9 shows the difference in temperature (1st column), salinity (2nd column) and vertical diffusivity (3rd
 348 column) between cvmix_KPP and fesom_KPP (cvmix_KPP minus fesom_KPP) averaged over five different
 349 depth ranges. The last column presents the fesom_KPP vertical diffusivity as a reference. Also here, the
 350 temperature and salinity differences are rather small compared to the climatological biases shown in Suppl.
 351 52. cvmix_KPP has the tendency to produce in the marginal seas of the AO a slightly fresher surface ocean,
 352 while the central AO shows an increase in salinity by ~0.1 psu.

353 The absolute value of the vertical diffusivity in fesom_KPP is larger than that in cvmix_KPP in the surface
 354 layers as well as in regions of unstable stratification (buoyancy frequency < 0), superimposed on a non-
 355 constant background diffusivity as described in Scholz et al., 2019. The different treatment of the squared
 356 velocity shear and buoyancy difference with respect to the surface in cvmix_KPP leads to a reduction of the

357 vertical diffusivity (3rd column) in the Labrador and Irminger Seas and to an increase in the AO locally by up
 358 to one order of magnitude (especially in the deep ocean).

359 The differences in MLD between fesom_KPP and cvmix_KPP are presented in Fig. 10, where and a) and b)
 360 show the absolute MLD value for fesom_KPP in the northern hemisphere in March and in the southern
 361 hemisphere in September respectively. Fig. 10 c) and d) display the corresponding anomalies between
 362 cvmix_KPP and fesom_KPP (cvmix_KPP-fesom_KPP). The absolute MLD values for fesom_KPP in March
 363 show high values of up to 3300 m in the entire LS and parts of the Irminger Sea, intermediate values of up to
 364 2000 m in the northern and eastern GIN seas and values of ~900m along the eastern continental slope of the
 365 North Atlantic. In the southern hemisphere in September, fesom_KPP simulates a large MLD of ~2500 m in
 366 the central Weddell Sea and weaker MLD of ~500 m in the band of the Antarctic Circumpolar Current
 367 (ACC). Compared to the fesom_KPP, cvmix_KPP leads to a ~200 m weaker MLD in the boundary currents
 368 of the LS, southern LS and along the northeastern continental slope of the GIN seas, and slightly larger MLD
 369 values in the IS and southwestern GIN Seas. The KPP ocean boundary layer depth (OBLd, Large et al. 1994)
 370 for fesom_KPP and the difference in OBLd between cvmix_KPP and fesom_KPP is additionally presented
 371 in Suppl. 7, where it is shown that cvmix_KPP produces a around 150 m shallower OBLd which is largely
 372 attributed to the different treatment of the surface quantities by averaging over 10% of the boundary layer
 373 depth.

374 Fig. 11 presents the differences in temperature (1st column), salinity (2nd column) and vertical diffusivity Kv
 375 (3rd column) between cvmix_PP and fesom_PP (cvmix_PP minus fesom_PP) as well as the absolute values
 376 of vertical diffusivity for fesom_PP (4th column). For the upper two surface depth ranges, cvmix_PP shows
 377 an overall small warming anomaly, except for the Gulf of Guinea in the 250-500 m depth range where the
 378 anomaly is negative. The salinity with cvmix_PP has overall slight positive anomalies, except for coastal
 379 Arctic areas and the Gulf of Guinea which indicate a slight freshening anomaly when compared to
 380 fesom_PP. The depth ranges below 500 m show no significant temperature or salinity differences between
 381 cvmix_PP and fesom_PP. The absolute value of Kv in fesom_PP ~~also shows~~ shows also larger values all over
 382 the surface layer as well as in the areas of unstable stratification similar to fesom_KPP, but with a lower
 383 magnitude and a more extended region of increased Kv in the LS and IS. The Kv difference between
 384 cvmix_PP and fesom_PP shows sporadically positive values along the coastal Arctic Ocean and in parts of
 385 the North Atlantic and GIN Seas. As one would expect, cvmix_PP has an order of magnitude larger values in
 386 the very deep ocean layer where the background viscosity enters the computation of Kv in cvmix_PP.

387 Fig. 12 presents the absolute and anomalous MLD between fesom_PP and cvmix_PP. The MLD in
 388 fesom_PP in March is deep in the entire LS and in parts of the IS, but slightly weaker and less spatially
 389 extended when compared to fesom_KPP (Fig. 10). The MLD in the GIN seas is very similar between
 390 fesom_PP and fesom_KPP. In the southern hemisphere the September MLD in fesom_PP shows a pattern in
 391 the central Weddell Sea which is similar to that in fesom_KPP, but shallower by ~500 m. The MLD
 392 difference between cvmix_PP and fesom_PP in the northern hemisphere indicates a very heterogeneous

393 pattern for the North Atlantic and in the southern hemisphere an up to ~150 m deeper MLD in the Weddell
 394 Sea MLD for cvmix_PP compared to fesom_PP. Overall, the difference in the simulation results induced by
 395 the difference in the two implementations of mixing schemes is generally small when considering the model
 396 biases relative to observations.

397 **3.3.2 Effects of tidal mixing parameterization of Simmons et al. (2004)**

398 | The tidal mixing parameterization of Simmons et al., (2004) provided by CVMix~~CVMIX~~ has been added to
 399 FESOM2.0. This mixing parameterization takes into account effects from internal wave generation due to
 400 tides over rough bottom topography. The breaking of internal waves in the vicinity of topographic features
 401 excites small-scale turbulence and leads to an enhanced vertical mixing. The tidal mixing parameterization
 402 uses a two dimensional map of tidal energy dissipation flux due to bottom drag and energy conversion into
 403 internal waves from Jayne and St. Laurent, (2001). It is transformed under consideration of a vertical
 404 redistribution function, the modelled buoyancy frequency and a tidal dissipation efficiency and mixing
 405 efficiency into a 3D map of diapycnal tidal vertical mixing, which is added to a primary vertical mixing
 406 scheme like PP, KPP or TKE. To show the effect of the tidal mixing parameterization we conducted a
 407 simulation using both cvmix_KPP and the tidal vertical mixing (cvmix_KPP_{TIDAL}). This simulation will be
 408 compared with a control run with cvmix_KPP in which the tidal mixing is not considered. The differences in
 409 temperature (1st column), salinity (2nd column) and vertical diffusivity Kv (3rd column) between
 410 cvmix_KPP_{TIDAL} and cvmix_KPP averaged over five different depth ranges are presented in Fig. 13. The last
 411 column of Fig. 13 shows the cvmix_KPP Kv as a reference. The temperature anomalies of the upper three
 412 depth ranges indicate that cvmix_KPP_{TIDAL} is colder especially in the marginal seas of the North Pacific, e.g.
 413 Sea of Japan, Sea of Okhotsk and Bering Sea, within the branch of the Gulf Stream (GS) and North Atlantic
 414 Current (NAC) as well as in the GIN- and Barents Seas. The Arctic Ocean shows a cooling anomaly for the
 415 500-1000 m and 1000-2000 m depth range. In the southern hemisphere the entire Southern Ocean is slightly
 416 colder when including the tidal vertical mixing. The tropical and subtropical ocean indicates a slight
 417 warming for cvmix_KPP_{TIDAL}.

418 The salinity anomalies between cvmix_KPP_{TIDAL} and cvmix_KPP show a pattern similar to that of the
 419 temperature, with a freshening in the marginal seas of the North Pacific, GS, NAC, GIN- and Barents Seas as
 420 well as for the Southern Ocean. The upper depth range indicates an increase in salinity for the AO, while the
 421 subsurface depth ranges show an AO freshening when including the tidal mixing. The tropical and
 422 subtropical ocean shows largely an increase in salinity under cvmix_KPP_{TIDAL}.

423 The difference in vertical diffusivity shows for cvmix_KPP_{TIDAL} an increase by an order of magnitude along
 424 the sloping bottom topography (e.g. the Midatlantic Ridge or Indonesian region) but also along the
 425 continental shelf regions~~all topographic features~~ which is induced by the tidal vertical mixing
 426 parameterization. On top of that the central AO shows a reduced vertical diffusivity by at least an order of
 427 magnitude for the 250-500 m, 500-1000 m and 1000-2000 m depth ranges, which comes from a change in
 428 local hydrography when including the tidal vertical mixing parameterization and the associated difference in

429 the KPP mixing scheme.

430 To further understand the effect of the tidal vertical mixing, Fig. 14 shows the global zonal mean temperature
 431 and salinity differences between the case of `cvmix_KPP` ~~and~~ the WOA18 (a, c) and the differences
 432 between `cvmix_KPPTIDAL` and `cvmix_KPP` (b, d). The temperature of `cvmix_KPP` shows a rather strong
 433 warming bias until 1000 m for the tropical and subtropical ocean as well as until ~2500 m for the ocean north
 434 of 50°N with respect to WOA18 (Fig. 14a). The deep ocean features small negative temperature anomalies
 435 for the tropical and subtropical ocean and slightly positive biases for the deep SO, when compared to
 436 WOA18. The salinity biases of the `cvmix_KPP` case (Fig. 14c) indicate a more heterogeneous but
 437 nevertheless similar picture. Also here positive salinity biases can be seen in the tropical and subtropical
 438 ocean until around 1000m as well as until ~2500m for the ocean north of 50°N. Looking at the temperature
 439 and salinity difference between `cvmix_KPPTIDAL` and `cvmix_KPP`, it can be seen that the tidal mixing of
 440 Simmons et al., (2004) leads to a cooling and freshening of the Southern Ocean and the ocean north of 50°N
 441 as well as a warming and salinification for the tropical and subtropical ocean until around 1500m. The deep
 442 ocean experiences a general slight warming and freshening due to the inclusion of the tidal mixing
 443 parameterization. In general one can summarize that the tidal mixing parameterization of Simmons et al.,
 444 (2004) helps to improve some of the biases with respect to WOA18. The last panel in Fig 14e shows the
 445 global zonal averaged vertical diffusivity profiles between `cvmix_KPPTIDAL` and `cvmix_KPP` and reveals a
 446 general strong increase in K_v along the continental slope in the southern ocean, in the northern hemisphere
 447 north of 50°N as well as in the deep ocean interior.

448 To illustrate the effect of Simmons et al., (2004) tidal mixing parameterization onto the MLD, Fig. 15
 449 presents the northern hemisphere ~~(March)~~~~Mareh~~ (a) and southern hemisphere ~~(September)~~~~September~~ (b)
 450 MLD in the case of `cvmix_KPP`, and the difference in MLD between `cvmix_KPPTIDAL` and `cvmix_KPP` also
 451 for northern hemisphere ~~(March)~~~~Mareh~~ (c) and southern hemisphere ~~(September)~~~~September~~ (d). In the
 452 northern hemisphere in March, tidal mixing leads to an increase in the MLD within the boundary currents of
 453 the LS, southern and eastern GIN Seas as well as in the Sea of Okhotsk. In the southern hemisphere
 454 ~~(September)~~~~September~~, tidal mixing leads to a significant ~1000 m increase in the Weddell Sea MLD. This
 455 significant increase originates largely from enhanced mixing of very cold surface waters along the
 456 continental slope of the Weddell Sea due to the tidal mixing parameterization. Suppl. 8 shows the KPP
 457 OBLd for `cvmix_KPP` and the difference in OBLd between `cvmix_KPP` with and without the tidal mixing of
 458 Simmons et al., (2004). It shows that with `cvmix_KPPTIDAL` the OBLd enhances especially in the western LS.

459

460 **3.3.3 Effects of Turbulent-Kinetic-Energy (TKE) mixing parameterisation**

461 More elaborate parameterizations of the vertical mixing in the ocean can be achieved by using closure
 462 schemes of turbulent kinetic energy (TKE) and the associated turbulent mixing within the mixed layer and
 463 below. One of these turbulent closure schemes is by Gaspar et al. (1990) that has been implemented via
 464 ~~CVMix~~~~CVMIX~~ (`cvmix_TKE`) into FESOM2.0 based on the work of Eden et al. (2014) and Gutjahr et al.

465 (2020). The turbulence closure scheme requires the solving of the second-order equation for TKE which is
 466 closed by connecting the vertical diffusivity with the turbulent kinetic energy and a length scale for its
 467 dissipation (Eden et al., 2014). For the background diffusivity we do not use ~~here~~ the latitude and depth
 468 dependent background diffusivity as in the previous mixing schemes. Instead, a constant minimum value of
 469 TKE is assumed, which takes into account the ocean interior mixing by internal wave breaking. To
 470 understand the effect of `cvmix_TKE` on oceanic hydrography, Fig. 16 presents the temperature and salinity
 471 biases of `cvmix_TKE` with respect to WOA18 (1st and 3rd column). To relate `cvmix_TKE` to the other vertical
 472 mixing schemes (e.g. KPP), the temperature and salinity differences between `fesom_KPP` and `cvmix_TKE`
 473 (2nd and 4th column) are shown as well. In general, the `cvmix_TKE` temperature and salinity biases with
 474 respect to WOA18 look largely very similar to the biases of `fesom_KPP` shown in Supp2. 1 (1st and 3rd
 475 column) in terms of the spatial patterns. A closer inspection of temperature and salinity differences between
 476 `cvmix_TKE` and `fesom_KPP` (Fig. 16+8, 2nd and 4th column) reveals that `cvmix_TKE` produces an up to
 477 0.5°C colder ocean within the 0-250 m, 250-500 m and 500-1000 m depth ranges in most of the ocean, a
 478 strong warming along the pathway of the NAC and the southern polar front in the South Atlantic, and small
 479 warming biases in the AO and SO. The salinity differences between `cvmix_TKE` and `fesom_KPP` indicate a
 480 salinification of the AO throughout the 0-250 m, 250-500 m and 500-1000 m depth ranges, but most
 481 pronounced in the surface depth range. The surface saline bias largely stems from reduced mixing under sea
 482 ice, which shields the ocean from the wind stress, a large source term of TKE. Furthermore, there are
 483 positive salinity anomalies in the North Atlantic (in the pathway of the GS and NAC), North Pacific and
 484 Southern Ocean, and largely negative salinity anomalies in the southern hemisphere. The temperature and
 485 salinity differences between `cvmix_TKE` and `fesom_KPP` in the depth ranges of 1000-2000 m and 2000-
 486 4000 m are rather marginal. It should be mentioned that a part of the anomalies described here could also be
 487 attributed to the different treatment of the background diffusivity. `fesom_KPP` takes a latitude and depth
 488 dependent value (Scholz et al., 2019), while `cvmix_TKE` assumes a constant value of minimum TKE on the
 489 surface ($10e-4 \text{ m}^2/\text{s}^2$) and for the interior mixing ($10e-6 \text{ m}^2/\text{s}^2$).

490 **3.3.4 Effects of energy consistent combination of TKE with the Internal Wave Dissipation** 491 **Energy and Mixing (IDEMIX) parameterisation**

492 Besides the standard implementation of vertical background diffusivity in `cvmix_TKE` using a constant
 493 minimum value of TKE to parameterize the effect of breaking of internal waves, `cvmix_TKE` also allows for
 494 the usage of a more sophisticated parameterization of internal wave breaking when combined with the
 495 IDEMIX parameterization (Olbers and Eden, 2013; Eden et al., 2014) which describes the energy transfer
 496 from sources towards sinks of internal waves by using a radiative transfer equation of weakly interacting
 497 internal waves. The resulting dissipation of energy is then treated as a source term in the turbulent kinetic
 498 energy balance equation leading at the end to an energetically more consistent interpretation of the internal
 499 ocean mixing process (Eden et al., 2014; Gutjahr et al., 2020). Thereby, IDEMIX solves for the propagation
 500 of low-mode internal waves far from their generation sites, which is considered by Fox-Kemper et al., (2019)

501 as one of the most difficult components of the internal wave energy budget. Different from the tidal mixing
 502 parameterization of Simmons et al., (2004), which only represents the generation of internal waves by
 503 barotropic tides and their breaking at rough topography, IDEMIX considers both the internal waves due to
 504 barotropic tides and the internal waves induced by wind-stress fluctuations and exiting at the base of the
 505 mixed layer (Gutjahr et al., 2020). The combination of cvmix_TKE and IDEMIX to improve the energetic
 506 consistency of ocean models is a rather new approach in the modelling community. It has been evaluated for
 507 stand-alone ocean models (Eden et al., 2014; Nielsen et al., 2018; Pollmann et al., 2017) and coupled models
 508 (Nielsen et al., 2019). Further, the computed TKE dissipation rates from IDEMIX have been evaluated
 509 against observational Argo float-derived dissipation rates by Pollmann et al. (2017) and have been found to
 510 be in good agreement (Gutjahr et al., 2019). In this part of the FESOM2 documentation, two FESOM2.0
 511 simulations with cvmix_TKE, one with and one without the usage of IDEMIX, are compared to assess the
 512 effect of IDEMIX on the modelled hydrography.

513 Fig. 17 presents the temperature (1st column), salinity (2nd column) and vertical diffusivity (3rd column)
 514 differences between cvmix_TKE with IDEMIX versus without it, averaged over five different depth layer
 515 ranges. As a reference the vertical diffusivity of cvmix_TKE without IDEMIX is also shown in the 4th
 516 column. The temperature differences indicate a clear warming of all equatorial and mid-latitude oceans
 517 and a cooling in the AO, SO and the marginal seas of the North Pacific throughout almost all the depth
 518 ranges, when cvmix_TKE is used with IDEMIX. There is a particularly strong warming in the surface and
 519 subsurface depth range of the North Atlantic, in the subsurface depth range of the south Pacific and in the
 520 deeper depth ranges of the Indian Ocean. The salinity differences (2nd column) have a similar spatial pattern,
 521 showing a rather strong salinification of the equatorial and mid-latitude global oceans and a freshening of
 522 the AO, SO and North Pacific from the surface to 500-1000 m depth range. The depth ranges below indicate
 523 a predominant general freshening almost everywhere, except for the Mediterranean outflow and Indian
 524 Ocean which indicate a slight **salinification** **warming**. The differences in the vertical diffusivity between
 525 cvmix_TKE with and without IDEMIX are only very small in the upper layer depth range. Therefore, all
 526 subsurface depth layers indicate considerable positive vertical diffusivity differences by up to two orders of
 527 magnitude especially along all major topographic features as well as in the SO. This shows in particular how
 528 IDEMIX parameterizes the vertical mixing due to the breaking of upwards propagating internal wave excited
 529 by barotropic tides along the ocean bottom topography but also the vertical mixing related to the internal
 530 wave breaking of downward propagating internal waves radiated out of the mixed layer like e.g. in the SO.

531 Fig. 18 presents the global zonal mean temperature and salinity differences of cvmix_TKE with respect to
 532 the WOA18 (a, c) as well as the temperature, salinity and vertical diffusivity differences between
 533 cvmix_TKE_{IDEMIX} and cvmix_TKE (b, d, e). The zonal mean temperature biases of cvmix_TKE with respect
 534 to WOA18 (Fig. 18a) are positive for the upper SO, the equatorial and mid-latitude oceans between 500m
 535 until 1000m, and the high-latitude ocean north of 60°N where the warming bias extends nearly from the
 536 surface until a depth of ~2500m. A rather weak warming bias is also present for the very deep >2500m SO.

537 General cooling biases can be seen for the equatorial and mid-latitude surface oceans, between a depth of
 538 ~1000m to 2000m as well as for the very deep ocean. The salinity biases for cvmix_TKE (Fig. 18c) show too
 539 high salinities for the high-latitude ocean north of 40°N and for the surface SO. Small salinity biases can be
 540 found in the equatorial and mid-latitude surface layers as well as around 40°N between ~1000 and 3000
 541 m.

542 The temperature differences between cvmix_TKE with and without IDEMIX (Fig. 18b) shows that the
 543 IDEMIX leads to a general warming of the equatorial and mid-latitude oceans especially between ~500 m
 544 and ~2000 m, but a cooling in the northern and southern high-latitude oceans. The salinity differences
 545 between cvmix_TKE with and without IDEMIX reveal a similar pattern with an increase in salinity for the
 546 equatorial and mid-latitude ocean from the surface until a depth ~2000m and a freshening bias in the same
 547 depth range for the high-latitude oceans and for the entire deep ocean as well.

548 The corresponding vertical diffusivity difference is shown in Fig. 18e. There, using IDEMIX results in an
 549 increase in vertical diffusivity along the bottom topographic slopes in the SO and north of 50°N until 70°N.
 550 Further, an increase in vertical diffusivity can be observed for almost the entire upper ocean until ~2000 m
 551 with deeper reaching positive anomalies between -60°S - 30°S and 30°N - 50°N. A reduction of the vertical
 552 diffusivity can be observed for the entire AO from the surface to bottom, for the equatorial and mid-
 553 latitude deep ocean >3000 m as well as for the deep (>4000 m) SO.

554 The effect of IDEMIX on the MLD is presented in Fig. 19, which shows the northern hemisphere
 555 ~~(March)March~~ a) and southern hemisphere ~~(September)September~~ b) cvmix_TKE MLD and the
 556 corresponding anomalies between cvmix_TKE with and without IDEMIX. It indicates that the use of
 557 IDEMIX leads to an increase in northern hemisphere MLD within the boundary currents of the LS by up to
 558 ~1000 m and in the southeastern GIN Seas by up to ~1800 m. In the southern hemisphere
 559 ~~(September)September~~, IDEMIX leads to a significant increase of the Weddell Sea MLD up to ~1800 m. We
 560 observe that using cvmix_KPP_{TIDAL} or cvmix_TKE_{IDEMIX} the model cannot maintain the upper halocline in the
 561 Weddell Sea. Hence the warm water that shall stay deep is exposed to the surface and the ocean loses heat. It
 562 can be well seen from Fig. 14.b and 18.b as blobs of negative temperature differences beneath the surface.
 563 As a consequence, the enlarged MLDs in the Weddell Sea appear. We therefore recommend to combine
 564 cvmix_KPP_{TIDAL}~~KPP_{TIDAL}~~ or cvmix_TKE_{IDEMIX} with the partial bottom cell approach, which has a partly
 565 compensating effect on the stratification in the Weddell Sea (see section 3.1 and Suppl. 3) and leads to a
 566 reduction of the MLD (Suppl. 9†) due to improvements of the current circulation in the Weddell Sea.

567 3.4 Implementation of Monin-Obukhov length dependent vertical mixing

568 In this section the effect of the Monin-Obukhov length vertical mixing (MOMIX) of Timmermann and
 569 Beckmann (2004) in FESOM2.0 is discussed. In an attempt to decrease the climatological biases especially
 570 in the Southern Ocean, which were otherwise prone to significant cooling and salinification (not shown),
 571 MOMIX has been implemented into FESOM2.0 as well. MOMIX serves as a parameterisation of the wind

572 driven mixing in the Southern Ocean, effective especially in the melting season, which helps to reduce
 573 winter deep convection in the Weddell Sea, thus affecting the basin wide ocean- and meridional overturning
 574 circulation (Timmermann and Beckmann, 2004). MOMIX computes the Monin-Obukhov length based on
 575 heat flux, freshwater flux, wind stress, sea ice concentration and sea ice velocity following the approach of
 576 Lemke (1987), and subsequently increases the vertical diffusivity within the Monin-Obukhov length to a
 577 value of $0.01\text{m}^2/\text{s}$.

578 Due to its success in reducing the aforementioned mean biases, MOMIX is applied at the moment in
 579 FESOM2.0 per default south of -50°S . In the following, the effects of MOMIX are discussed, based on
 580 simulation of fesom_KPP and cvmix_TKE each with and without MOMIX.

581 Fig. 20 presents the temperature (1st and 2nd column) and salinity (3rd and 4th column) differences between
 582 simulations with and without MOMIX for both the fesom_KPP and cvmix_TKE schemes, averaged over
 583 five different depth ranges. Using MOMIX in the Southern Ocean leads to a significant warming of up to
 584 1°C for almost the entire Southern Ocean south of -60°S throughout all considered depth ranges, except for
 585 the surface depth range of the southern Weddell Sea and subsurface southern Pacific which exhibits cooling
 586 anomalies. The warming anomaly is slightly more pronounced for fesom_KPP than cvmix_TKE. The usage
 587 of MOMIX in the Southern Ocean leads in fesom_KPP to a warming of the Gulf Stream and to a cooling of
 588 the NAC. For cvmix_TKE this behaviour is reversed. The salinity anomalies indicate a freshening for the
 589 entire Southern Ocean surface depth range when using MOMIX, while the subsurface depth ranges indicate
 590 predominantly a slight increase in salinity, except for the southern Weddell Sea 250-500m depth range.

591 To emphasize the effect of MOMIX on the Weddell Sea MLD, Fig. 21 presents the Southern Ocean
 592 September MLD for fesom_KPP (a) and cvmix_TIDAL (b) without MOMIX and the corresponding
 593 anomalies with minus without MOMIX (c, d). The MLD for fesom_KPP (a) and cvmix_TKE (b) are very
 594 large over the entire Weddell Sea and parts of the Ross Sea. The MLD values are higher and more extended
 595 with fesom_KPP than with cvmix_TKE. However, for both vertical mixing schemes without using MOMIX,
 596 the MLD values are way too high within the Weddell Sea and Ross Sea. The figures c) and d) visualize what
 597 happens with the Southern Ocean MLD for fesom_KPP and cvmix_TKE when MOMIX is used. Especially
 598 for fesom_KPP, MOMIX leads to a significant decrease in the MLD in almost the entire Weddell Sea of up
 599 to ~ 3000 m, except for the southwestern Weddell Sea close to the continental shelf which exhibits an
 600 increase in MLD. Also the large MLD patch in the Ross Sea becomes strongly reduced when using MOMIX.
 601 Both fesom_KPP and cvmix_TKE face the same pattern in MLD reduction when using MOMIX, only the
 602 magnitude in the MLD decrease is larger in fesom_KPP than in cvmix_TKE.

603 Since MOMIX has a rather strong effect in reducing the Weddell Sea open-ocean deep-water formation it
 604 will also consequently affect the formation of Antarctic Bottom Water (AABW) and the Meridional
 605 Overturning Circulation (MOC). Fig. 22 shows the fesom_KPP global (a), Atlantic (b) and Pacific (c) MOC
 606 when MOMIX is switched off and the difference from the case with MOMIX (bottom row). It can be seen
 607 that on a global but also basin-wide scale, the use of MOMIX leads to a reduction in the strength of the

608 AABW, in the Atlantic by ~ 0.6 Sv and in the Pacific by up to ~ 1.7 Sv. Also the strength of the upper AMOC
 609 cell is reduced by ~ 1 Sv when using MOMIX. We conclude that using MOMIX helps to alleviate the
 610 problem of large MLDs in the Weddell Sea which we addressed above. Hence, the options `cvmix_KPPTIDAL`
 611 or `cvmix_TKEIDEMIX` are strongly recommended to be used in combination with MOMIX, which is per
 612 default active only South of -50°S .

613

614 4 Discussion and Conclusions

615 This paper describes the two new features -- partial cells and embedded sea ice introduced to FESOM2.0 and
 616 the implementation of the vertical mixing library `CVMix`~~`CVMix`~~ (`cvmix_PP`, `cvmix_KPP`, `cvmix_TKE`,
 617 `IDEMIX` and `cvmix_TIDAL`), together with the elaboration of the effect of MOMIX. These new features
 618 expand the functionality of FESOM2.0, its applicability and its ability to be better compared to other state of
 619 the art ocean general circulation models. With its model components implemented, FESOM2.0 is mature for
 620 its practical applications and holds its leading role in the competition of the global unstructured ocean
 621 models.

622 We demonstrate the effect of using partial cells by comparing them against the full cell approach. It is shown
 623 that partial cells lead to an improved representation of the Gulf Stream branch, with a reduction in the cold
 624 bias in the northwest corner of the North Atlantic associated with an improved NAC pathway. Further,
 625 partial cells lead to a “northwest corner like” meridional deflection of the NAC between -30°W and -15°W
 626 which is still too far east, but leads to an improved representation in a rather coarse configuration which
 627 would otherwise be dominated by a rather zonal NAC. Partial cells also lead to a general speed up of the
 628 boundary currents shown as an example for the North Atlantic.

629 The improvement of the NAC pathway and the speedup of the boundary currents especially in the subpolar
 630 gyre by using partial cells is described by a variety of publications (e.g. Barnier et al., 2006; Käse et al.,
 631 2001; Myers, 2002). Besides all its advantages, partial cells also harbor the risk of increasing the existing
 632 biases, like in our coarse configuration the deep Arctic warm bias, which is largely inherited from the
 633 Atlantic Water inflow branch that expands too deep. The tendency of partial cells to increase the velocity in
 634 the boundary currents leads to an enhancement of the Atlantic Water inflow to the Arctic Ocean. As the
 635 temperature in the Arctic Atlantic Water layer is already overestimated without using partial cells, the warm
 636 bias becomes even larger when partial cells are used. However, this is not the principle drawback of partial
 637 cells, but rather an issue of model tuning for the pan-Arctic region, which is part of our on-going work (for
 638 example, evaluating different numerical schemes of momentum viscosity). In the southern hemisphere, using
 639 partial cells leads to a significant reduction of the otherwise rather high MLD in the Weddell Sea. Regarding
 640 the configuration used in this paper, using partial cells leads to a strengthening of the warm deep water
 641 current (Vernet et al. 2019) that crosses the Weddell Sea interior. Thus it enhances the local stratification
 642 (see Suppl. 3† white arrow) and reduces vertical convection. It can be summarized that the usage of partial

643 cells clearly improves the general circulation within FESOM2.0 and that the benefits outweigh the
 644 drawbacks.

645

646 The second feature that was presented, is the effect of embedded sea ice vs. the standard case of levitating
 647 sea ice. Embedded sea ice allows for a further step towards a more realistic and physical ocean-sea ice
 648 interaction by adding the sea ice loading to the ocean pressure. This has the potential of increasing ocean
 649 variability especially near the sea ice edge. Our results indicate that the embedded sea ice has only a minor
 650 effect on the sea ice distribution itself. Nevertheless the effect is the strongest for the Northern Hemisphere
 651 summer, when the sea ice edge retracts towards the Arctic Ocean interior. Here embedded sea ice leads to an
 652 up to 9% increase in the sea ice concentration in the eastern Arctic Ocean marginal seas, which also leads to
 653 an increase in the bias of the sea ice edge, and to a 6% decrease in the marginal seas of the western Arctic
 654 Ocean, which slightly reduces the sea ice extent bias there. The effect of embedded sea ice on the
 655 hydrography of the Arctic Ocean is much more significant, with an increase in temperature and salinity of up
 656 to 0.5°C and 0.1psu, respectively through most of the upper 1000 m. The increase in temperature and salinity
 657 is connected to a particular increase of the boundary currents especially along the eastern boundaries of the
 658 Eurasian Basin but also to a strengthening of the cyclonic current along the Lomonosov Ridge, which was
 659 otherwise rather weakly represented in the levitating sea ice case. The deficiencies of the Arctic Ocean
 660 currents representation in our model configuration can be partially attributed to the rather coarse resolution.
 661 However, with embedded sea ice we seem to be able to at least partly counteract the effect of low resolution
 662 and improve the Arctic Ocean current structure at rather low costs. We note that embedded sea ice could also
 663 deteriorate the model results in some cases. Since the boundary currents around the Eurasian Basin get
 664 enhanced, the already existing Atlantic Water layer biases get enhanced. However, as mentioned above, this
 665 is an issue of model tuning with this coarse resolution setup, not a drawback of embedded sea ice itself.

666

667 To further expand the functionality and comparability of FESOM2.0 we implemented the vertical mixing
 668 library ~~CVMix~~**CVMIX** and its components, which in our implementation include `cvmix_PP`, `cvmix_KPP`,
 669 `cvmix_TIDAL`, `cvmix_TKE` and `cvmix_TKE+IDEMIX`. At first, the vertical mixing parameterizations
 670 `fesom_KPP` and `fesom_PP`, which have been already implemented in FESOM2.0, are briefly evaluated. It is
 671 shown that `fesom_PP` produces a slightly colder tropical and subtropical but warmer polar oceans on the
 672 surface, with a largely warmer ocean below the surface layer depth range, when compared to `fesom_KPP`.
 673 This makes between these two, `fesom_KPP` the preferred vertical mixing option at least in terms of mean
 674 temperature biases. In terms of salinity biases, `fesom_PP` performs better in the surface and subsurface AO
 675 as well as in the equatorial Atlantic and Indian Ocean, while otherwise `fesom_KPP` indicates smaller biases.
 676 In the next instance, `fesom_KPP` and `cvmix_KPP` have been compared to each other, since there are slight
 677 differences in their implementation. The difference in implementation leads only to minor differences in
 678 temperature throughout all considered depth ranges. Regarding the salinity differences, `cvmix_KPP` produces

679 a considerably fresher surface AO compared to fesom_KPP, which is attributed to a reduced near surface
680 vertical diffusivity in cvmix_KPP that leads to an over-stabilisation of the AO halocline. This enhances the
681 mean salinity bias in that region. In terms of vertical diffusivity, cvmix_KPP has the tendency to produce by
682 up to one order of magnitude lower value (especially in the very deep depth range) in the main convection
683 areas of Labrador Sea and Greenland Sea, throughout all considered depth ranges, accompanied by increased
684 diffusivity in the subsurface of the Arctic Ocean. The reduced diffusivity in the main convection areas is
685 attributed to the different treatment of the shear- and buoyancy difference with respect to the surface in
686 cvmix_KPP that leads to a reduction of the local ocean boundary layer depth and to slightly reduced
687 maximum MLD in Labrador and Greenland Sea, while the maximum MLD in the Weddell Sea becomes
688 slightly enhanced, when using cvmix_KPP over fesom_KPP.

689 Since the implementation of cvmix_PP and fesom_PP are also slightly different, we also compare them.
690 Although the produced diffusivities between cvmix_PP and fesom_PP are very similar, cvmix_PP indicates
691 a further warming and salinification in the surface and 250-500 m depth ranges except for the upwelling
692 region in the Gulf of Guinea which indicates a cooling and freshening and the surface depth range of the
693 Arctic Ocean where it creates a predominant freshening, when compared the fesom_PP. The MLD values
694 indicate that cvmix_PP leads in FESOM2.0 to a slightly stronger convection in the Weddell Sea. The
695 differences between fesom_PP and cvmix_PP are related to the different treatment of the background
696 coefficient for viscosity when computing the diffusivity see Pacanowski and Philander (1981).

697 The effect of implementing cvmix_TIDAL in combination with cvmix_KPP was further assessed.
698 cvmix_TIDAL serves here as a resourceful way to heterogenize the effect of tidally induced internal wave
699 breaking that is otherwise homogenized in a constant or latitude dependent value for the background
700 diffusivity. Using cvmix_TIDAL clearly leads to an enhancement of the vertical diffusivity along the slopes
701 of the bottom topography, where tidally related internal wave breaking is induced. This leads especially in
702 the high-latitude marginal seas, e.g. Sea of Okhotsk and Bering Sea but also Arctic Ocean and Southern
703 Ocean, to a decrease in temperature and salinity due to the enhanced mixing along their shelves. This enables
704 cvmix_TIDAL to improve some of the existing local temperature and salinity biases within FESOM2.0 at
705 rather low computational costs. However, the enhanced vertical diffusivity along the shelf of the Weddell
706 Sea weakens the stratification and leads to a further increase in the MLD of the Weddell Sea of up to 1000
707 m.

708 Further, the implications of TKE vertical mixing parameterisation in FESOM2.0, added by Eden et al. (2014)
709 and Gutjahr et al. (2020) to the ~~CVMIX~~ **CVMix** library, was evaluated based on a comparison with
710 fesom_KPP. It is shown that the mean temperature and salinity differences between cvmix_TKE (Fig. 17)
711 and fesom_KPP (Fig. 9) show very similar patterns. cvmix_TKE tends to produce a generally colder tropical
712 and extratropical ocean together with slightly warmer polar oceans when compared to fesom_KPP. The
713 salinity differences between cvmix_TKE and fesom_KPP shows that cvmix_TKE tends to produce a
714 significantly saltier surface layer AO, revealing a much smaller salinity bias for the Arctic Ocean interior.

715 This is largely connected to enhanced surface vertical mixing along the Arctic Ocean shelf break (not shown)
716 within `cvmix_TKE`, that helps to partly destabilize the AO halocline. The improvement of the Arctic Ocean
717 hydrography when using `cvmix_TKE` is also found by Gutjahr et al. (2020) in the coupled ocean-atmosphere
718 Max Planck Institute Earth System Model (MPI-ESM1.2). Further, `cvmix_TKE` leads to a salinity increase in
719 the entire North Atlantic and northwest Pacific marginal seas, while the southern hemisphere, except for the
720 Southern Ocean, shows a freshening when compared to `fesom_KPP`. The reduced temperatures and salinities
721 in the tropics and extratropics when using `cvmix_TKE` are connected to the reduced vertical mixing.
722 However the regions of strong vertical shear, e.g. the branch of the Gulf Stream and NAC as well as
723 Southern Ocean show stronger vertical mixing in `cvmix_TKE`, when compared to `fesom_KPP` (not shown),
724 which is accompanied by positive temperature and salinity anomalies between `cvmix_TKE` and `fesom_KPP`.
725 Following the comparison of `cvmix_TKE` and `fesom_KPP`, a side by side comparison of `cvmix_TKE` with
726 and without IDEMIX was carried out. Here IDEMIX provides an alternative formulation of the background
727 diffusivity in `cvmix_TKE` using a radiative transfer equation of weakly interacting internal waves (Olbers
728 and Eden 2013), where energy is transferred from sources of internal waves to wave sinks, such as the
729 breaking of internal waves, which provide a source for TKE, leading to an energetically more consistent
730 treatment of internal mixing (Eden et al. 2014). As compared to the tidal background mixing
731 parameterization of Simmons et al (2004), IDEMIX allows not only for the generation of internal waves by
732 barotropic tides interacting with marine topography, but also for their propagation in the horizontal and
733 vertical directions away from region of generation and their damping due to wave-wave interaction or
734 interaction with the continental shelf. Further, IDEMIX allows for the excitation of internal waves at the base
735 of the mixed layer by high frequency wind forcing (Eden et al. 2014).

736 The combined TKE + IDEMIX approach was already applied in a couple of publications (Eden et al. 2014,
737 Nielsen et al. 2018, Gutjahr et al. 2020). It was shown in Pollmann et al. 2017 that TKE dissipation rates
738 from the combined TKE+IDEMIX approach are comparable to dissipation rates estimated from Argo floats.
739 In FESOM2.0, the usage of TKE+IDEMIX leads to a significant increase in the tropical and extratropical,
740 and to a decrease in the high-latitude, temperature and salinity over depth when compared to the case of only
741 using `cvmix_TKE`. These differences compensate for some of the biases in the surface and intermediate
742 depth ranges when IDEMIX is not used. The usage of IDEMIX leads to an enhanced heterogeneous
743 representation of vertical mixing especially below the mixed layer along the continental shelves and
744 topographic slopes. However the temperature gain for the deeper depth ranges below 1000 m seems to be
745 strongly overestimated when using `cvmix_TKE+IDEMIX`, hinting at a too strong vertical mixing in the deep
746 ocean. When it comes to the MLD, `cvmix_TKE+IDEMIX` leads in the northern hemisphere to a significant
747 increase in the MLD along the Labrador Sea boundary currents and in the southern GIN seas, which can be
748 attributed to the enhanced mixing along the continental slope of the North Atlantic and in the vicinity of the
749 overflow regions. In the southern hemisphere using IDEMIX leads to an enhancement of the vertical
750 diffusivity along the continental slope of the Weddell Sea. This leads to an enhanced mixing of cold and

751 salty waters, which further reduces the stratification and significantly increases the MLD of the Weddell Sea
752 and to a rather overestimation of the otherwise already high MLD values.

753 This is in contrast to the findings of Gutjahr et al. 2020, who found that in their coupled MPI-ESM1.2
754 simulation, IDEMIX led to a reduction of the vertical mixing in the Weddell Sea allowing for more local
755 stratification. ~~One~~ possibility to overcome the lack of performance of IDEMIX but also of cvmix_TIDAL
756 in the Southern Ocean and Weddell Sea could be its combination with partial bottom cells, which had the
757 tendency to significantly reduce the deep convection in the Weddell Sea. At this point it needs further studies
758 also with FESOM2.0 to analyse the different behaviour of IDEMIX that could be influenced by local
759 resolution, coupled ocean-atmosphere feedback or just different background water mass structure.
760 Nevertheless, the achievable energetic consistency with the combined cvmix_TKE+IDEMIX approach is an
761 interesting feature that should find more applications in the ocean modelling community, although there is
762 still some way to go to better understand and improve its integration.

763 The last part in this paper deals with the vertical mixing parameterisation MOMIX of Timmermann and
764 Beckmann, (2004) in FESOM2.0 that helped us to overcome some major biases in the model. Since the very
765 beginning of FESOM2.0 the model suffered from a severe cooling and salinification bias in the Southern
766 Ocean and marginal seas around Antarctica, that was accompanied by a strongly overestimated MLD values
767 and too weak stratification in the Weddell Sea. It is shown here that applying MOMIX south of -50°S helped
768 to significantly reduce the biases and bring the MLD depth values in the Weddell Sea into a reasonable
769 range. MOMIX increases the vertical diffusivity within the depth range of the Monin-Obukhov mixing
770 length. This helps the warmer and fresher surface water masses from the melting season to connect with
771 colder and saltier subsurface water masses from the freezing season and thus increase the stratification and
772 reduce the vertical convection. Further, the using of MOMIX in combination with fesom_KPP leads to a
773 cooling and freshening in the branch of the NAC that seemed to be connected to a weakening of the upper
774 AMOC cell by 1 Sv and thus to a slight reduction of the meridional heat transport. The reason why
775 FESOM2.0 in the Southern Ocean is so dependent on MOMIX, which was not the case with FESOM1.4,
776 needs further research. Our actual best practise FESOM2.0 configuration uses the zstar approach with partial
777 cells and MOMIX switched on as a default, together with fesom_KPP for the vertical mixing, although
778 cvmix_TKE + IDEMIX shows some promising improvements especially for Arctic applications.

779 To summarize, this paper is the second part of the documentation of the development of important key
780 components of FESOM2.0 in a realistic global model configuration. We described the implementation of
781 partial cells and embedded sea ice and their impact on the modelled hydrography. Furthermore, we briefly
782 described the already existing vertical mixing parameterisation of fesom_KPP and fesom_PP as well as the
783 newly introduced mixing parameterization of cvmix_PP, cmix_KPP, cmix_TIDAL, cvmix_TKE and
784 cvmix_TKE+IDEMIX that came with the incorporation of the vertical mixing library ~~CVMix~~~~CVMIX~~ into
785 FESOM2.0.

786 **5 Code availability**

787 The FESOM2.0 version used to carry out the simulations reported here is available on zenodo through
 788 <https://doi.org/10.5281/zenodo.4742242>. The used mesh, as well as the temperature, salinity and vertical
 789 velocity (for the calculation of the MOC) data of all conducted simulations, can be found under
 790 https://swiftbrowser.dkrz.de/tcl_s/hituvPNH3xwiIy/FESOM2.0_evaluation_part2_scholz_etal. Simulated
 791 results can of course also be obtained from the authors upon request. Mesh partitioning in FESOM2.0 is
 792 based on a METIS version 5.1.0 package developed at the Department of Computer Science and Engineering
 793 at the University of Minnesota (<http://glaros.dtc.umn.edu/gkhome/views/metis>, last access: 18 November
 794 2019). METIS and the pARMS solver (Li et al., 2003) present separate libraries which are freely available
 795 subject to their licenses. The Polar Science Center hydrographic climatology (Steele et al., 2001) used for
 796 model initialization and the CORE-II atmospheric forcing data (Large and Yeager, 2009) is freely available
 797 online. The vertical mixing library [CVMix](https://github.com/CVMix/CVMix) ~~CVMIX~~ is freely available from
 798 <https://github.com/CVMix/CVMix-src> or <https://doi.org/10.5281/zenodo.1000801>
 799

800 **Author contributions**

801 SD, DS, PS and NK worked on the development of the FESOM2.0 model code and the tuning of the model.
 802 All simulations shown in this paper were carried out by PS who were also responsible for preparing the basic
 803 manuscript. QW, SD, NK, DS and TJ have contributed to the final version of the manuscript.

804 **Acknowledgements**

805 This paper is a contribution to the project S2: Improved parameterisations and numerics in climate models,
 806 S1: Diagnosis and Metrics in Climate Models and M5: Reducing spurious diapycnal mixing in ocean models
 807 of the Collaborative Research Centre TRR 181 “Energy Transfer in Atmosphere and Ocean” funded by the
 808 Deutsche Forschungsgemeinschaft (DFG, German Research Foundation) – project no. 274762653, and the
 809 Helmholtz initiative REKLIM (Regional Climate Change). This study has benefited from funding from the
 810 Initiative and Networking Fund of the Helmholtz Association through the project “Advanced Earth System
 811 Modelling Capacity (ESM)”. Dmitry Sein was also supported in the framework of the state assignment of the
 812 Ministry of Science and Higher Education of Russia (№0128-2021-0014).

813 **References**

814

815 Adcroft, A. and Campin, J.-M.: Rescaled height coordinates for accurate representation of free-surface flows in ocean
 816 circulation models, *Ocean Model.*, 7(3–4), 269–284, doi:10.1016/j.ocemod.2003.09.003, 2004.

- 817 Adcroft, A., Hill, C. and Marshall, A. J.: Representation of topography by shaved cells in a height coordinate ocean
818 model, *Mon. Weather Rev.*, 125(9), 2293–2315, doi:10.1175/1520-0493(1997)125<2293:ROTBSC>2.0.CO;2, 1997.
- 819 Barnier, B., Madec, G., Penduff, T., Molines, J.-M., Treguier, A., Le Sommer, J., Beckmann, A., Biastoch, A., Böning,
820 C., Dengg, J., Derval, C., Durand, E., Gulev, S., Remy, E., Talandier, C., Theetten, S., Maltrud, M., McClean, J. and De
821 Cuevas, B.: Impact of partial steps and momentum advection schemes in a global ocean circulation model at eddy-
822 permitting resolution, *Ocean Dyn.*, 56(5–6), 543–567, doi:10.1007/s10236-006-0082-1, 2006.
- 823 Campin, J. M., Marshall, J. and Ferreira, D.: Sea ice-ocean coupling using a rescaled vertical coordinate z^* , *Ocean*
824 *Model.*, 24(1–2), 1–14, doi:10.1016/j.ocemod.2008.05.005, 2008.
- 825 Cavalieri, D. J., Parkinson, C. L., Gloersen, P. and Zwally, H. J.: ea Ice Concentrations from Nimbus-7 SMMR and
826 DMSP SSM/I-SSMIS Passive Microwave Data, Version 1. [Indicate subset used], , doi:10.5067/8GQ8LZQVL0VL,
827 1996.
- 828 Cox, M. D.: A numerical ocean model with improved bottom topographic representation, GFDL/NOAA Tech. Rep., 27
829 pp. [Available from Princet. Univ. Princeton, New Jersey 08540.], 1977.
- 830 [Danabasoglu, G., Yeager, S. G., Bailey, D., Behrens, E., Bentsen, M., Bi, D., Biastoch, A., Böning, C., Bozec, A.,](#)
831 [Canuto, V. M., Cassou, C., Chassignet, E., Coward, A. C., Danilov, S., Diansky, N., Drange, H., Farneti, R., Fernandez,](#)
832 [E., Fogli, P. G., Forget, G., Fujii, Y., Griffies, S. M., Gusev, A., Heimbach, P., Howard, A., Jung, T., Kelley, M., Large,](#)
833 [W. G., Leboissetier, A., Lu, J., Madec, G., Marsland, S. J., Masina, S., Navarra, A., George Nurser, A. J., Pirani, A., y](#)
834 [Mélia, D. S., Samuels, B. L., Scheinert, M., Sidorenko, D., Treguier, A. M., Tsujino, H., Uotila, P., Valcke, S.,](#)
835 [Voldoire, A. and Wang, Q.: North Atlantic simulations in Coordinated Ocean-ice Reference Experiments phase II](#)
836 [\(CORE-II\). Part I: Mean states, *Ocean Model.*, 73, 76–107, doi:10.1016/j.ocemod.2013.10.005, 2014.](#)
- 837 Danilov, S., Sidorenko, D., Wang, Q. and Jung, T.: The Finite-volumE Sea ice–Ocean Model (FESOM2), *Geosci.*
838 *Model Dev.*, 10(2), 765–789, doi:10.5194/gmd-10-765-2017, 2017.
- 839 Eden, C. and Olbers, D.: An energy compartment model for propagation, nonlinear interaction, and dissipation of
840 internal gravity waves, *J. Phys. Oceanogr.*, 44(8), 2093–2106, doi:10.1175/JPO-D-13-0224.1, 2014.
- 841 Eden, C., Czeschel, L. and Olbers, D.: Toward Energetically Consistent Ocean Models, *J. Phys. Oceanogr.*, 44, 3160–
842 3184, doi:10.1175/JPO-D-13-0260.1, 2014.
- 843 Ferrari, R., Griffies, S. M., Nurser, A. J. G. and Vallis, G. K.: A boundary-value problem for the parameterized
844 mesoscale eddy transport, *Ocean Model.*, 32(3–4), 143–156, doi:10.1016/j.ocemod.2010.01.004, 2010.
- 845 Fox-kemper, B., Adcroft, A., Böning, C. W., Chassignet, E. P., Gerdes, R., Greatbatch, R. J., Griffies, S. M. and
846 Hallberg, R. W.: Challenges and Prospects in Ocean Circulation Models, , 6(February), 1–29,
847 doi:10.3389/fmars.2019.00065, 2019.
- 848 Fox-Kemper, B. and Menemenlis, D.: Can large eddy simulation techniques improve mesoscale rich ocean models?, in
849 *Ocean Modeling in an Eddy Regime*, Volume 177, edited by M. W. Hecht and H. Hasumi, pp. 319–337., 2008.
- 850 Gaspar, P., Goris, Y. G. R. I. and Lefevre, J.: A Simple Eddy Kinetic Energy Model for Simulations of the Oceanic
851 Vertical Mixing ’ Tests at Station Papa and Long-Term Upper Ocean Study Site, , 95, 179–193, 1990.
- 852 Gent, P. R. and McWilliams, J. C.: Isopycnal Mixing in Ocean Circulation Models, *J. Phys. Oceanogr.*, 20(1), 150–155,
853 doi:10.1175/1520-0485(1990)020<0150:IMIOCM>2.0.CO;2, 1990.
- 854 Gent, P. R., Willebrand, J., McDougall, T. J. and McWilliams, J. C.: Parameterizing Eddy-Induced Tracer Transports in
855 Ocean Circulation Models, *J. Phys. Oceanogr.*, 25(4), 463–474, doi:10.1175/1520-
856 0485(1995)025<0463:PEITTI>2.0.CO;2, 1995.
- 857 Griffies, S. M., Böning, C., Bryan, F. O., Chassignet, E. P., Gerdes, R., Hasumi, H., Hirst, A., Treguier, A. M. and
858 Webb, D.: Developments in ocean climate modelling, *Ocean Model.*, 2(3–4), 123–192, doi:10.1016/s1463-

859 5003(00)00014-7, 2000.

860 Griffies, S. M., Levy, M., Adcroft, A. J., Danabasoglu, G., Hallberg, R. W., Jacobsen, D., Large, W. and Ringler, T.:
861 Theory and numerics of the Community Ocean Vertical Mixing (CVMix) project., 2015.

862 Gutjahr, O., Putrasahan, D., Lohmann, K., Jungclaus, J. H., Von Storch, J. S., Brüggemann, N., Haak, H. and Stössel,
863 A.: Max Planck Institute Earth System Model (MPI-ESM1.2) for the High-Resolution Model Intercomparison Project
864 (HighResMIP), *Geosci. Model Dev.*, 12(7), 3241–3281, doi:10.5194/gmd-12-3241-2019, 2019.

865 Gutjahr, O., Brüggemann, N., Haak, H., Jungclaus, J. H. Putrasahan, D. A. Lohmann, K. and von Storch, J.-S.:
866 Comparison of ocean vertical mixing schemes in the Max Plank Institute Earth System Model (MPI-ESM1.2), *Geosci.*
867 *Model Dev.*, in review, doi:https://doi.org/10.5194/gmd-2020-202, 2020.

868 [Hibler, W., Heil, P. and Lytle, V. I.: On simulating high frequency variability in Antarctic sea-ice dynamics models.](#)
869 [Ann. Glaciol., 27, 443-448, 1998.](#)

870 [Hutchings, J. K., Heil, P. and Hibler, W. D.: Modeling Linear Kinematic Features in Sea Ice, Mon. Wea. Rev., 3481-](#)
871 [3497, https://doi.org/10.1175/MWR3045.1, 2005.](#)

872 Ilicak, M., Drange, H., Wang, Q., Gerdes, R., Aksenov, Y., Bailey, D., Bentsen, M., Biastoch, A., Bozec, A., Böning,
873 C., Cassou, C., Chassignet, E., Coward, A. C., Curry, B., Danabasoglu, G., Danilov, S., Fernandez, E., Fogli, P. G.,
874 Fujii, Y., Griffies, S. M., Iovino, D., Jahn, A., Jung, T., Large, W. G., Lee, C., Lique, C., Lu, J., Masina, S., George
875 Nurser, A. J., Roth, C., Salas y Méliá, D., Samuels, B. L., Spence, P., Tsujino, H., Valcke, S., Voldoire, A., Wang, X.
876 and Yeager, S. G.: An assessment of the Arctic Ocean in a suite of interannual CORE-II simulations. Part III:
877 Hydrography and fluxes, *Ocean Model.*, 100, 141–161, doi:10.1016/j.ocemod.2016.02.004, 2016.

878 Jayne, S. R. and St. Laurent, L. C.: Tidal Dissipation over Rough, *Geophys. Res. Lett.*, 28(5), 811–814, 2001.

879 Käse, R. H., Biastoch, A. and Stammer, D. B.: On the mid-depth circulation in the Labrador and Irminger Seas,
880 *Geophys. Res. Lett.*, 28(18), 3433–3436, doi:10.1029/2001GL013192, 2001.

881 Large, W. G. and Yeager, S. G.: The global climatology of an interannually varying air - Sea flux data set, *Clim. Dyn.*,
882 33(2–3), 341–364, doi:10.1007/s00382-008-0441-3, 2009.

883 Large, W. G., McWilliams, J. C. and Doney, S. C.: Oceanic vertical mixing: A review and a model with a nonlocal
884 boundary layer parameterization, *Rev. Geophys.*, 32(4), 363, doi:10.1029/94RG01872, 1994.

885 Lemke, P.: A coupled one-dimensional sea ice-ocean model, , 92(C12), 164–172,
886 doi:https://doi.org/10.1029/JC092iC12p13164, 1987.

887 Locarnini, R. A., Mishonov, A. V., Baranova, O. K., Boyer, T. P., Zweng, M. M., Garcia, H. E., Reagan, J. R., Seidov,
888 D., Weathers, K., Paver, C. R. and Smolyar, I.: World Ocean Atlas 2018, Volume 1: Temperature, A. Mishonov Tech.
889 Ed.; NOAA Atlas NESDIS 81, 52, 2018.

890 Maier-Reimer, E., Mikolajewicz, U. and Hasselmann, K.: Mean circulation of the Hamburg LSG OGCM and its
891 sensitivity to the thermohaline surface forcing, *J. Phys. Oceanogr.*, 23(4), 731–757, doi:10.1175/1520-
892 0485(1993)023<0731:MCOTHL>2.0.CO;2, 1993.

893 [Marshall, J. and Schott, F.: Open-ocean convection: Observations, theory, and models, Rev. Geophys., 37\(1\), 1–64,](#)
894 [doi:10.1029/98RG02739, 1999.](#)

895 Myers, P. G.: SPOM: A regional model of the sub-polar north Atlantic, *Atmos. - Ocean*, 40(4), 445–463,
896 doi:10.3137/ao.400405, 2002.

897 Nielsen, S. B., Jochum, M., Eden, C. and Nuterman, R.: An energetically consistent vertical mixing parameterization in
898 CCSM4, *Ocean Model.*, 127, 46–54, doi:10.1016/j.ocemod.2018.03.002, 2018.

899 Nielsen, S. B., Jochum, M., Pedro, J. B., Eden, C. and Nuterman, R.: Two-Timescale Carbon Cycle Response to an

- 900 AMOC Collapse, *Paleoceanogr. Paleoclimatology*, 34(4), 511–523, doi:10.1029/2018PA003481, 2019.
- 901 Olbers, D. and Eden, C.: A Global Model for the Diapycnal Diffusivity Induced by Internal Gravity Waves, , 1759–
902 1779, doi:10.1175/JPO-D-12-0207.1, 2013.
- 903 Pacanowski, R. C. and Gnanadesikan, A.: Transient response in a Z-level ocean model that resolves topography with
904 partial cells, *Mon. Weather Rev.*, 126(12), 3248–3270, doi:10.1175/1520-0493(1998)126<3248:TRIAZL>2.0.CO;2,
905 1998.
- 906 Pacanowski, R. C. and Philander, S. G. H.: Parameterization of Vertical Mixing in Numerical Models of Tropical
907 Oceans, *J. Phys. Oceanogr.*, 11(11), 1443–1451, doi:10.1175/1520-0485(1981)011<1443:POVMIN>2.0.CO;2, 1981.
- 908 Pollmann, F., Eden, C. and Olbers, D.: Evaluating the Global internal wave model IDEMIX using finestructure
909 methods, *J. Phys. Oceanogr.*, 47(9), 2267–2289, doi:10.1175/JPO-D-16-0204.1, 2017.
- 910 Redi, M. H.: Oceanic Isopycnal Mixing by Coordinate Rotation, *J. Phys. Oceanogr.*, 12(10), 1154–1158,
911 doi:10.1175/1520-0485(1982)012<1154:OIMBCR>2.0.CO;2, 1982.
- 912 Robertson, R. and Dong, C.: An evaluation of the performance of vertical mixing parameterizations for tidal mixing in
913 the Regional Ocean Modeling System (ROMS), *Geosci. Lett.*, 6(1), 1–18, doi:10.1186/s40562-019-0146-y, 2019.
- 914 Rousset, C., Vancoppenolle, M., Madec, G., Fichefet, T., Flavoni, S., Barthélemy, A., Benshila, R., Chanut, J., Levy,
915 C., Masson, S. and Vivier, F.: The Louvain-La-Neuve sea ice model LIM3.6: Global and regional capabilities, *Geosci.*
916 *Model Dev.*, 8(10), 2991–3005, doi:10.5194/gmd-8-2991-2015, 2015.
- 917 [Sallée, J. B., Shuckburgh, E., Bruneau, N., Meijers, A. J. S., Bracegirdle, T. J. and Wang, Z.: Assessment of Southern](#)
918 [Ocean mixed-layer depths in CMIP5 models: Historical bias and forcing response, *J. Geophys. Res. Ocean.*, 118\(4\),](#)
919 [1845–1862, doi:10.1002/jgrc.20157, 2013.](#)
- 920 Scholz, P., Sidorenko, D., Gurses, O., Danilov, S., Koldunov, N., Wang, Q., Sein, D., Smolentseva, M., Rakowsky, N.
921 and Jung, T.: Assessment of the Finite-volume Sea ice-Ocean Model (FESOM2.0) -- Part 1: Description of selected key
922 model elements and comparison to its predecessor version, *Geosci. Model Dev.*, 12(11), 4875–4899, doi:10.5194/gmd-
923 12-4875-2019, 2019.
- 924 Semmler, T., Danilov, S., Gierz, P., Goessling, H. F., Hegewald, J., Hinrichs, C., Koldunov, N., Khosravi, N., Mu, L.,
925 Rackow, T., Sein, D. V., Sidorenko, D., Wang, Q. and Jung, T.: Simulations for CMIP6 With the AWI Climate Model
926 AWI-CM-1-1, *J. Adv. Model. Earth Syst.*, 12(9), 1–34, doi:10.1029/2019MS002009, 2020.
- 927 Semtner, A. J. and Mintz, Y.: Numerical simulation of the Gulf Stream and mid-ocean eddies., *J. Phys. Oceanogr.*, 7(2,
928 Mar. 1977), 208–230, doi:10.1175/1520-0485(1977)007<0208:nsotgs>2.0.co;2, 1977.
- 929 Shchepetkin, A. F.: A method for computing horizontal pressure-gradient force in an oceanic model with a nonaligned
930 vertical coordinate, *J. Geophys. Res.*, 108(C3), 3090, doi:10.1029/2001JC001047, 2003.
- 931 Simmons, H. L., Jayne, S. R., St, L. C. and Weaver, A. J.: Tidally driven mixing in a numerical model of the ocean
932 general circulation, , 6, 245–263, doi:10.1016/S1463-5003(03)00011-8, 2004.
- 933 Steele, M., Morley, R. and Ermold, W.: PHC: A global ocean hydrography with a high-quality Arctic Ocean, *J. Clim.*,
934 14(9), 2079–2087, doi:10.1175/1520-0442(2001)014<2079:PAGOHW>2.0.CO;2, 2001.
- 935 Timmermann, R. and Beckmann, A.: Parameterization of vertical mixing in the Weddell Sea, *Ocean Model.*, 6(1), 83–
936 100, doi:10.1016/S1463-5003(02)00061-6, 2004.
- 937 Van Roekel, L., Adcroft, A. J., Danabasoglu, G., Griffies, S. M., Kauffman, B., Large, W., Levy, M., Reichl, B. G.,
938 Ringler, T. and Schmidt, M.: The KPP Boundary Layer Scheme for the Ocean: Revisiting Its Formulation and
939 Benchmarking One-Dimensional Simulations Relative to LES, *J. Adv. Model. Earth Syst.*, 10(11), 2647–2685,
940 doi:10.1029/2018MS001336, 2018.

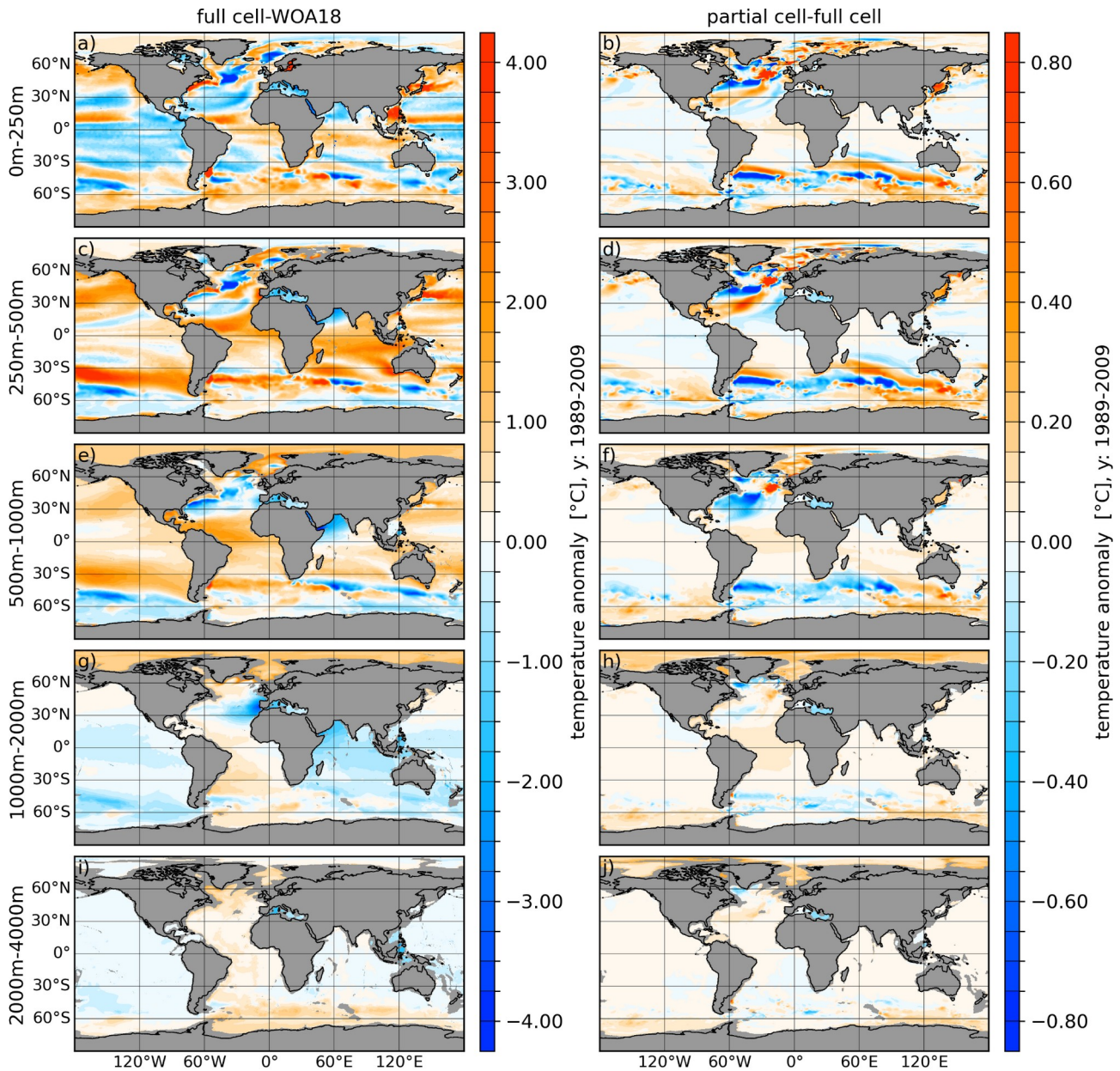
941 Vernet, M., Geibert, W., Hoppema, M., Brown, P. J., Haas, C. and Hellmer, H. H.: The Weddell Gyre , Southern
 942 Ocean : Present Knowledge and Future Challenges Reviews of Geophysics, *Rev. Geophys.*, 57, 623–708,
 943 doi:10.1029/2018RG000604, 2019.

944 Wang, Q., Danilov, S., Sidorenko, D., Timmermann, R., Wekerle, C., Wang, X., Jung, T. and Schröter, J.: The Finite
 945 Element Sea Ice-Ocean Model (FESOM) v.1.4: formulation of an ocean general circulation model, *Geosci. Model Dev.*,
 946 7(2), 663–693, doi:10.5194/gmd-7-663-2014, 2014.

947

948 Zweng, M. M., Reagan, J. R., Seidov, D., Boyer, T. P., Locarnini, R. A., Garcia, H. E., Mishonov, A. V., Baranova, O.
 949 K., Weathers, K., Paver, C. R. and Smolyar, I.: World Ocean Atlas 2018, Volume 2: Salinity, A. Mishonov Tech. Ed.;
 950 NOAA Atlas NESDIS 82, 50, 2018.

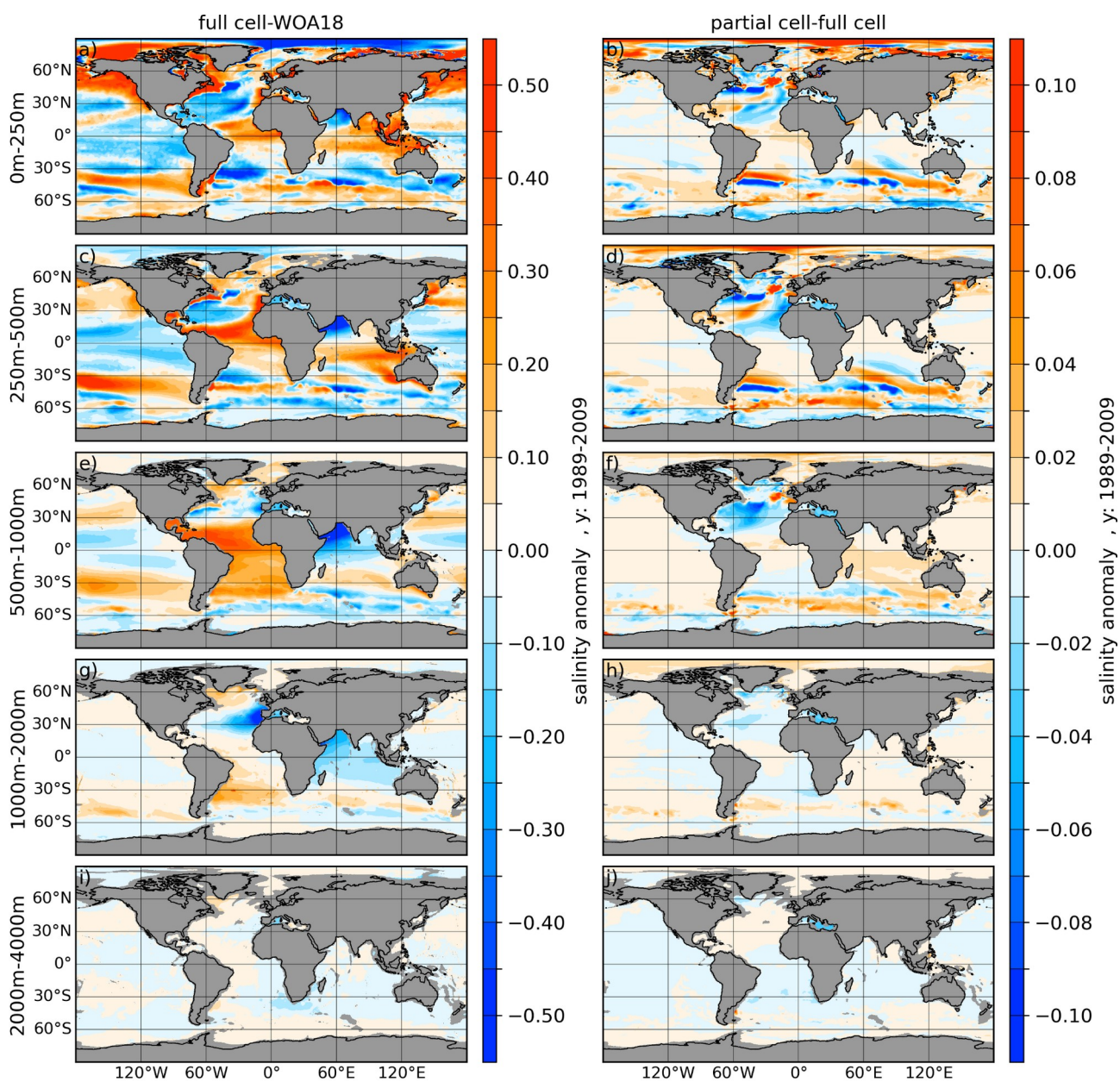
951



952

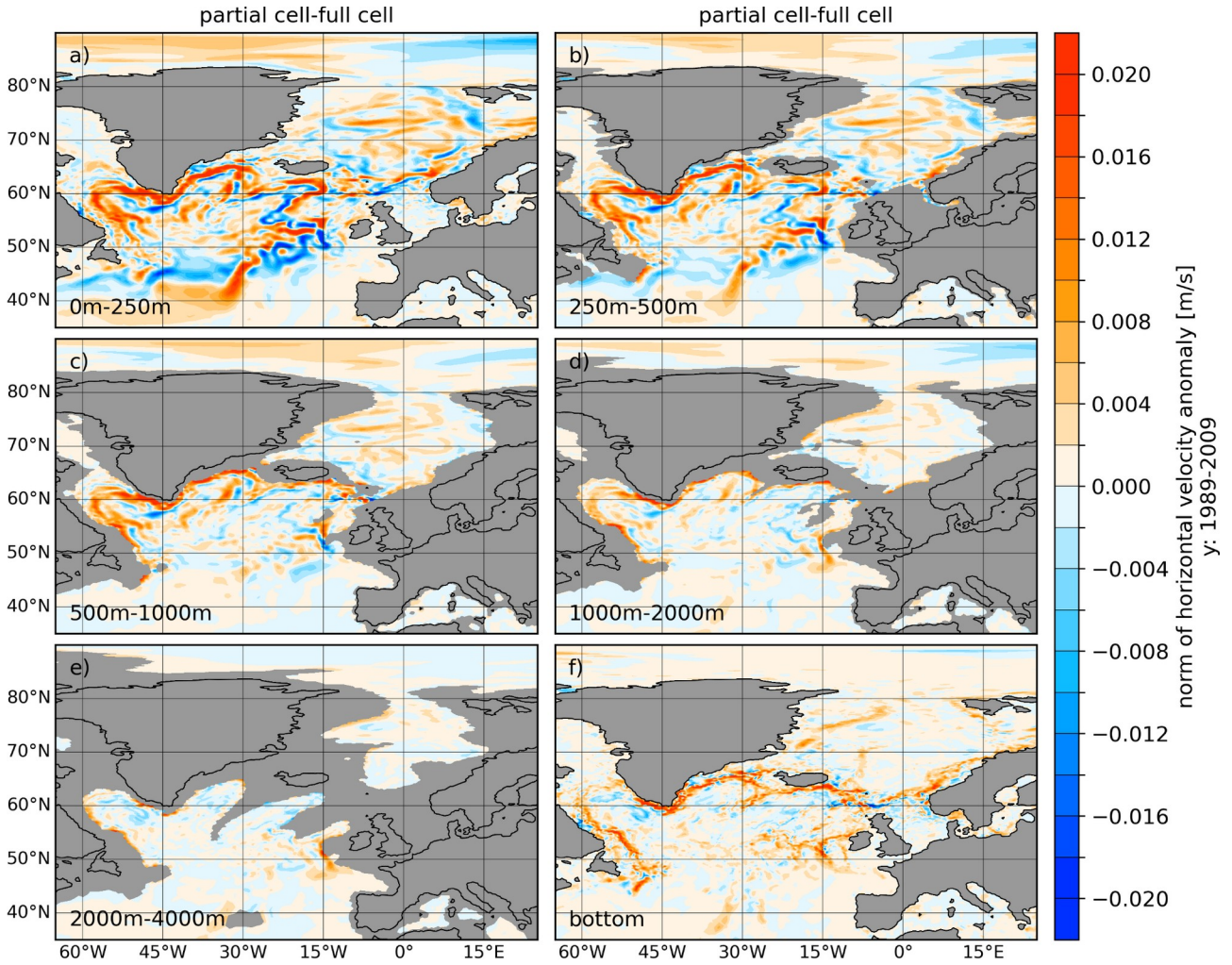
953 **Figure 1:** (Left column) Temperature biases full cells referenced to the World Ocean Atlas 2018 (WOA18,
 954 Zweng et. al 2018) averaged over the period 1989-2009. The right column shows the temperature difference
 955 between partial and full cells (partial minus full). From top to bottom the panels show the vertically averaged
 956 fields for the depth ranges of 0-250 m, 250-500 m, 500-1000 m, 1000-2000 m and 2000-4000 m.

55
957
958

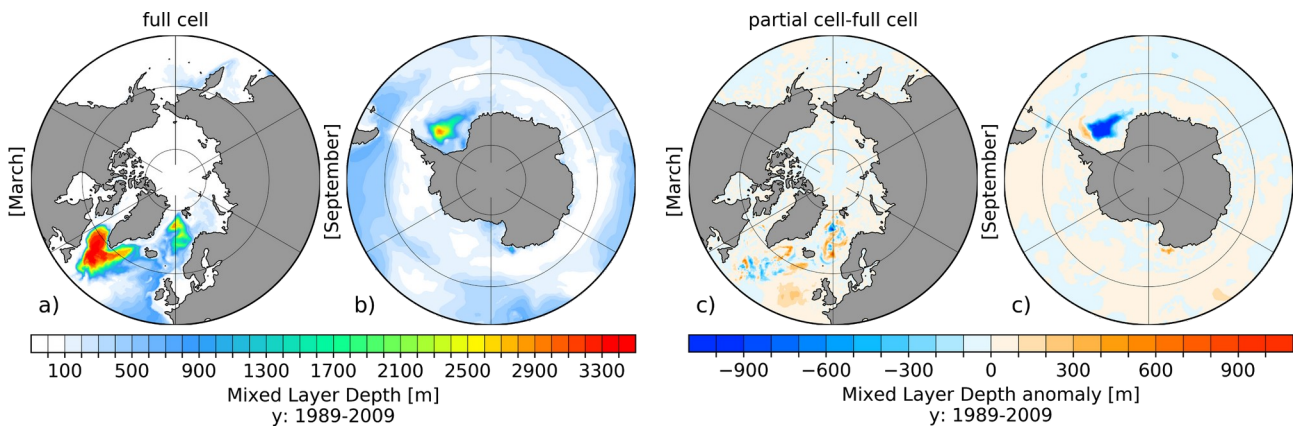


959
960

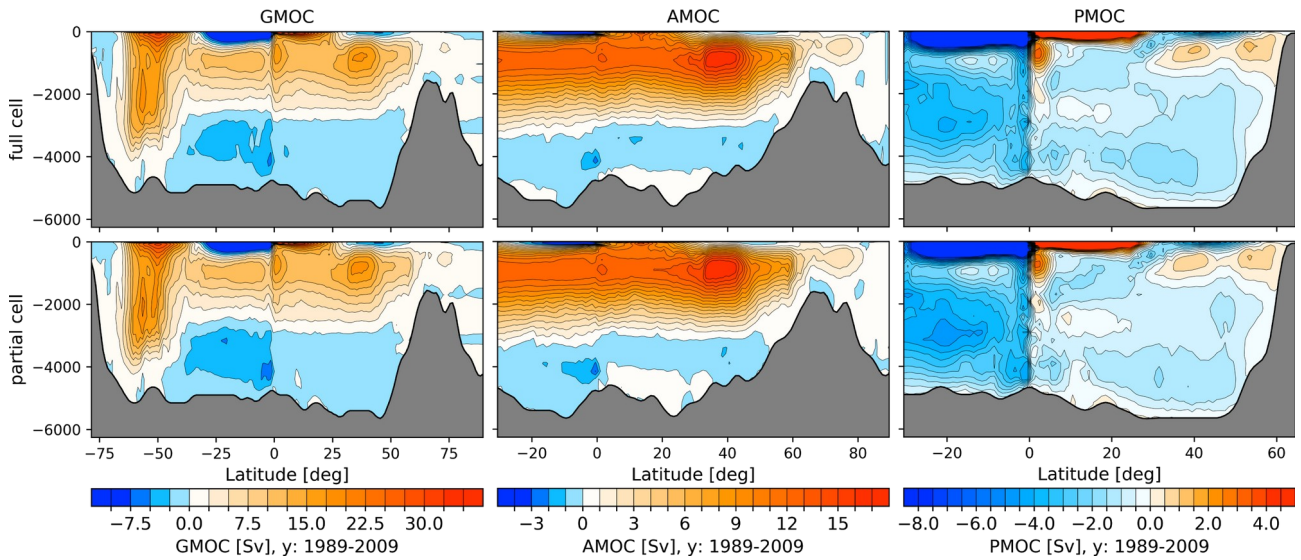
Figure 2: Same as Fig. 1, but for salinity.



961
962 **Figure 3:** Difference of the horizontal velocity norm between simulations with partial and full cells (partial-
963 full) averaged over the period 1989-2009 and averaged over the depth ranges of 0-250 m, 250-500 m, 500-
964 1000 m, 1000-2000 m and 2000-4000 m as well as the bottom value.
965
966



967
968 **Figure 4:** Northern hemispheric March (a) and southern Hemispheric September (b) mixed layer depth
969 (MLD) with full cells as well as corresponding anomalous MLD with partial minus full cells (c, d), averaged
970 for the period 1989-2009.

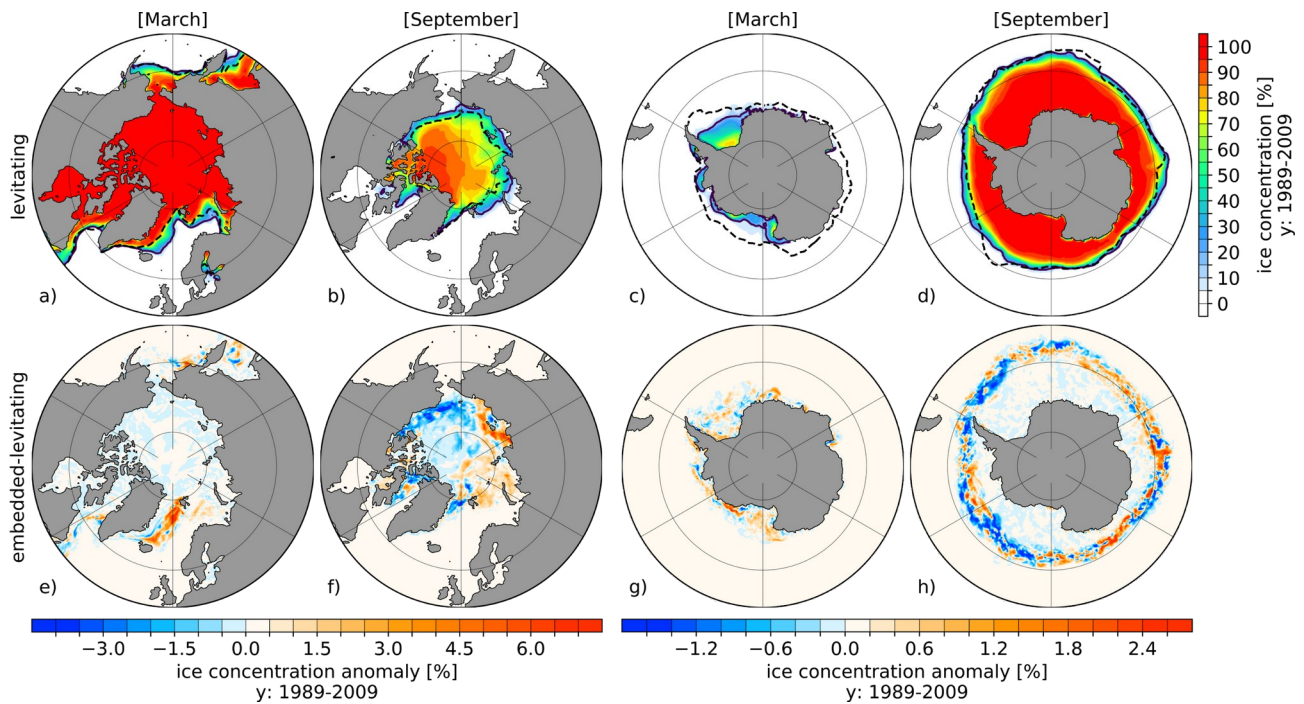


971

972 **Figure 5:** Global (GMOC, left column), Atlantic (AMOC, middle column) and Indo-Pacific (PMOC, right
 973 column) Meridional Overturning Circulation for full cell (upper row) and partial cell (lower row) averaged
 974 for the time period 1989-2009.

975

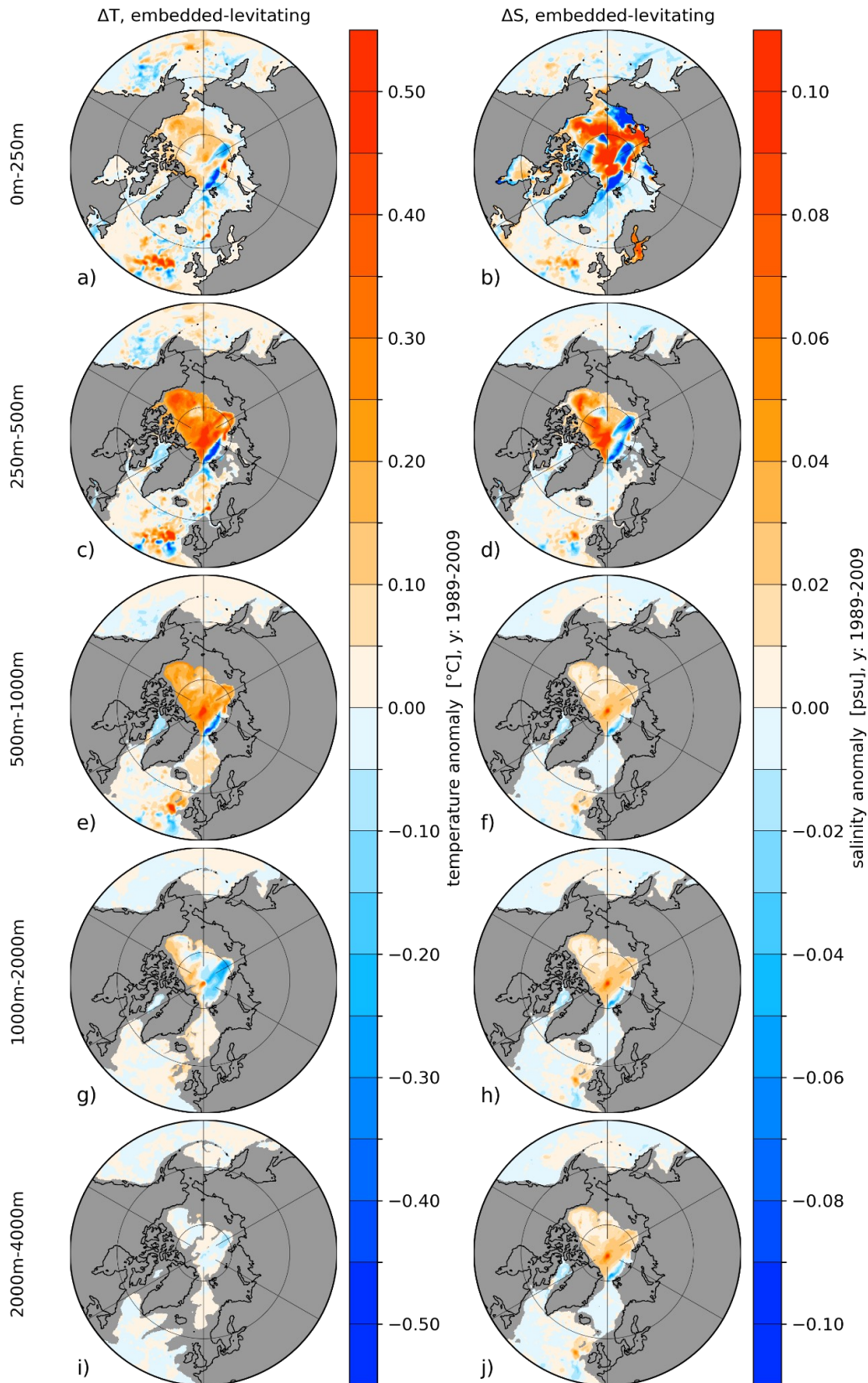
976



977

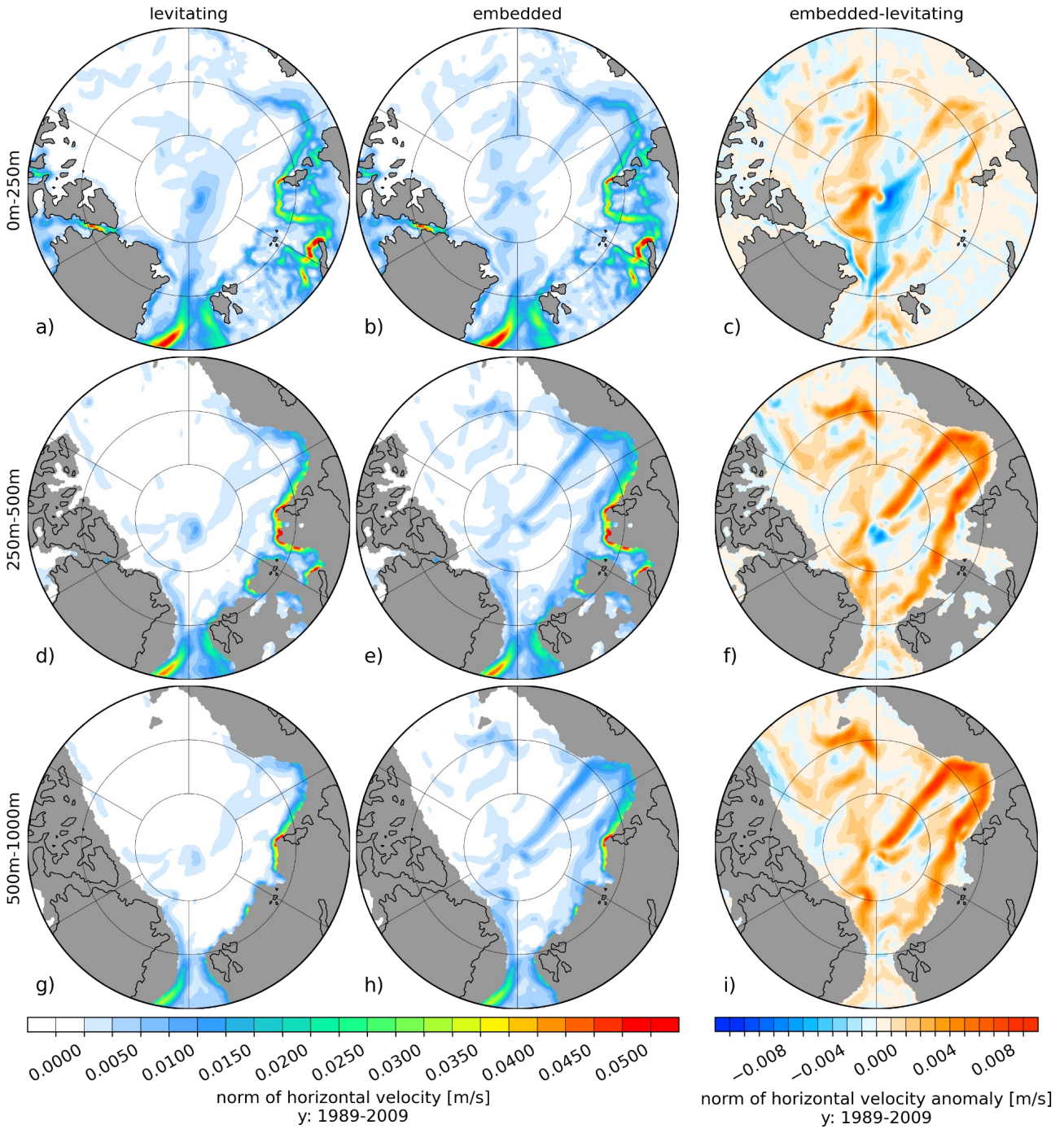
978 **Figure 6:** Levitating (upper row) northern and southern hemispheric March (a, c) and September (b, d) sea
 979 ice concentration averaged for the period 1989-2009. Solid and dashed lines indicate the simulated and
 980 observed (Cavaliere et al., 1996) contour of the 15% sea ice extent. The lower row shows the corresponding
 981 sea ice concentration anomalies between embedded and levitating sea ice (embedded minus levitating)
 982 averaged over the same period.

983



984

985 **Figure 7:** Temperature (left column) and salinity (right column) difference between embedded- and
 986 levitating sea ice averaged for the period 1989 to 2009. From top to bottom, panels show the vertically
 987 averaged fields for the depth ranges of 0-250 m, 250-500 m, 500-1000 m, 1000-2000 m and 2000-4000 m.
 988



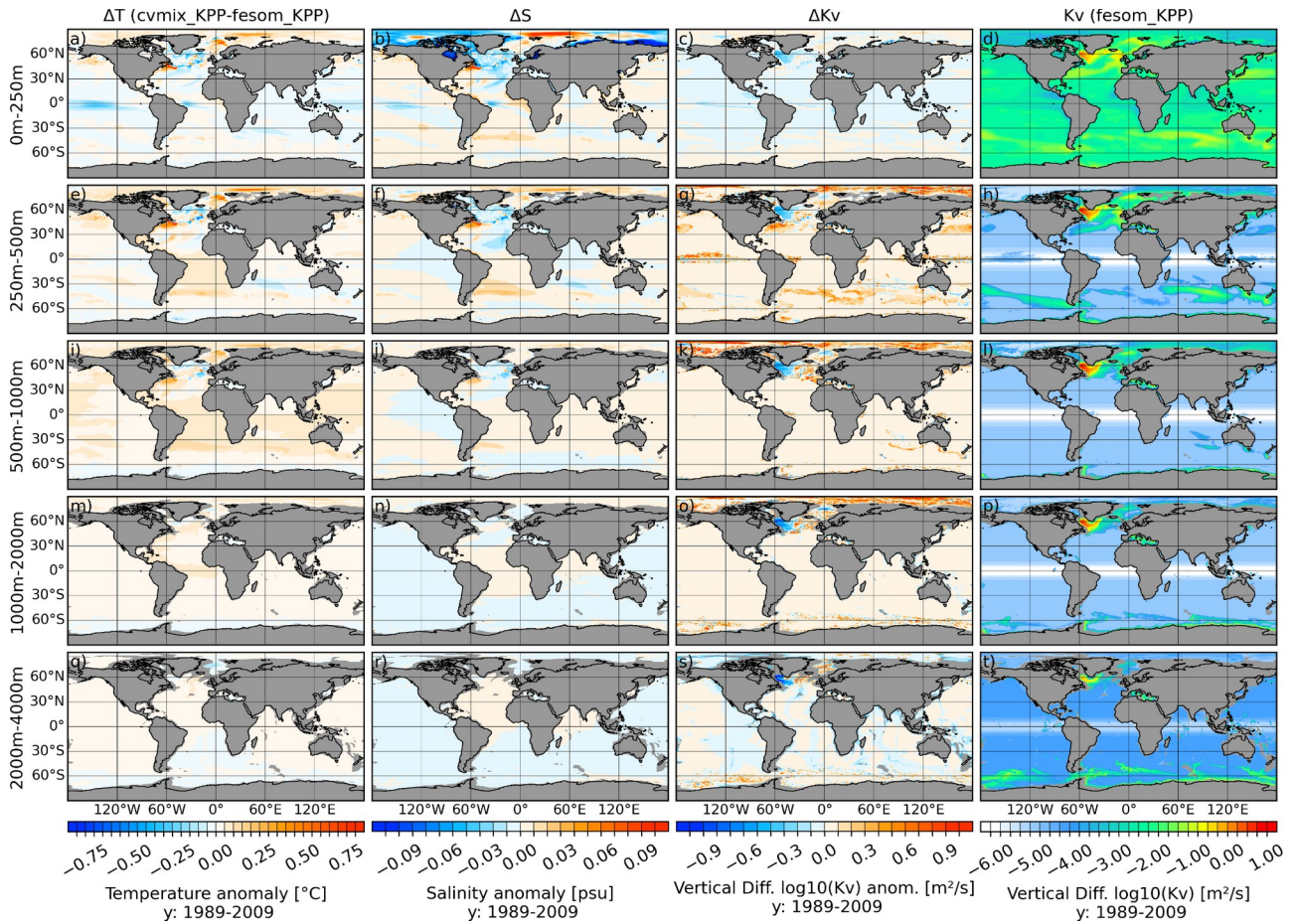
989

990 **Figure 8:** Norm of ocean velocity for levitating (left column) and floating (middle column) and the
 991 difference between embedded and levitating (right column) sea ice averaged for the period 1989 to 2009.
 992 From top to bottom, the panels show the vertically averaged fields for the depth ranges of 0-250 m, 250-500
 993 m and 500-1000 m.

994

995

996

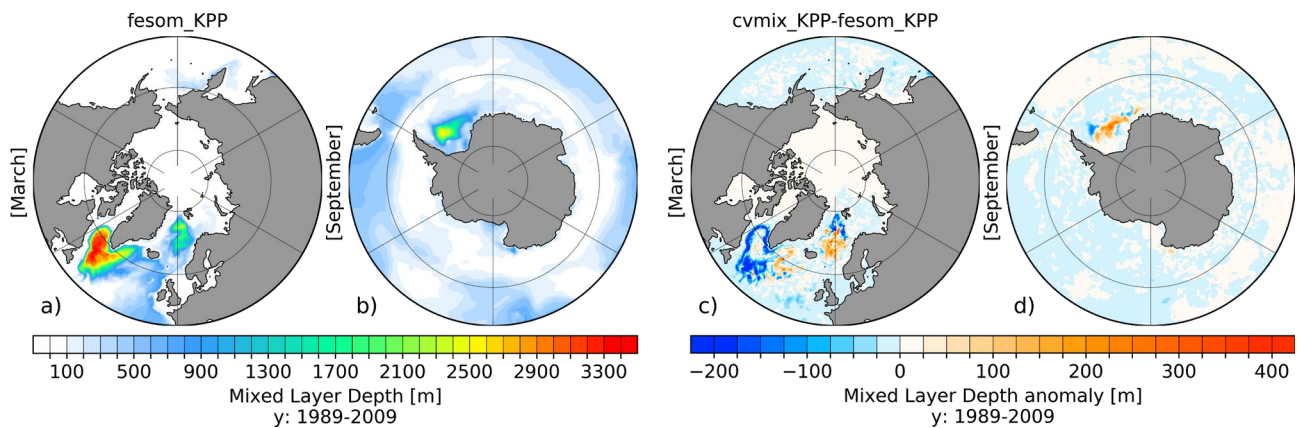


997

998 **Figure 9:** Temperature (1st Column), salinity (2nd column) and vertical diffusivity (3rd column) difference
 999 between *cvmix_KPP* and original *fesom_KPP* implementation as well as the absolute vertical diffusivity
 1000 values (4th column) for *fesom_KPP* averaged for the period 1989 to 2009. From top to bottom, panels show
 1001 the vertically averaged fields for the depth ranges of 0-250 m, 250-500 m, 500-1000 m, 1000-2000 m and
 1002 2000-4000 m.

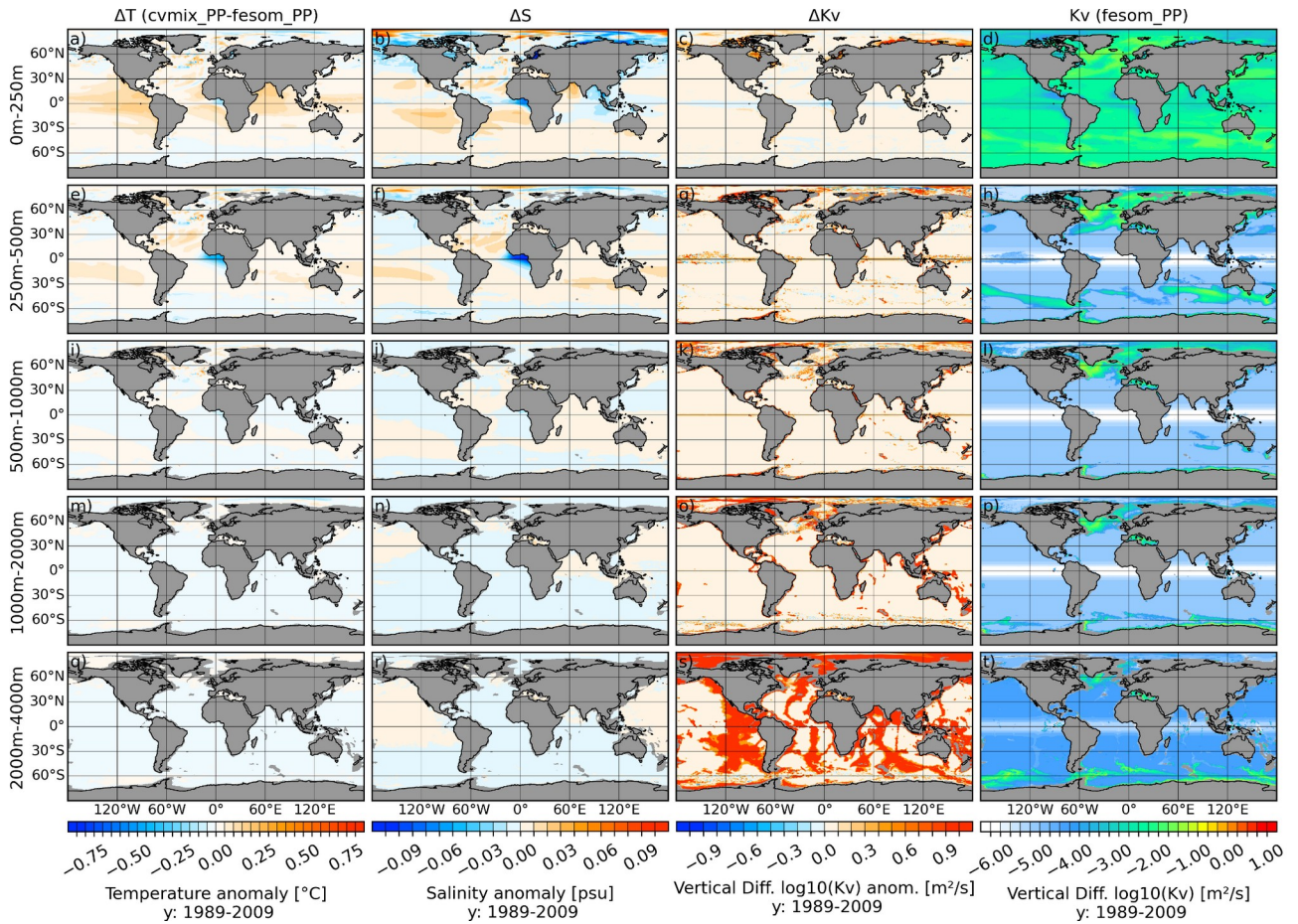
1003

1004



1005

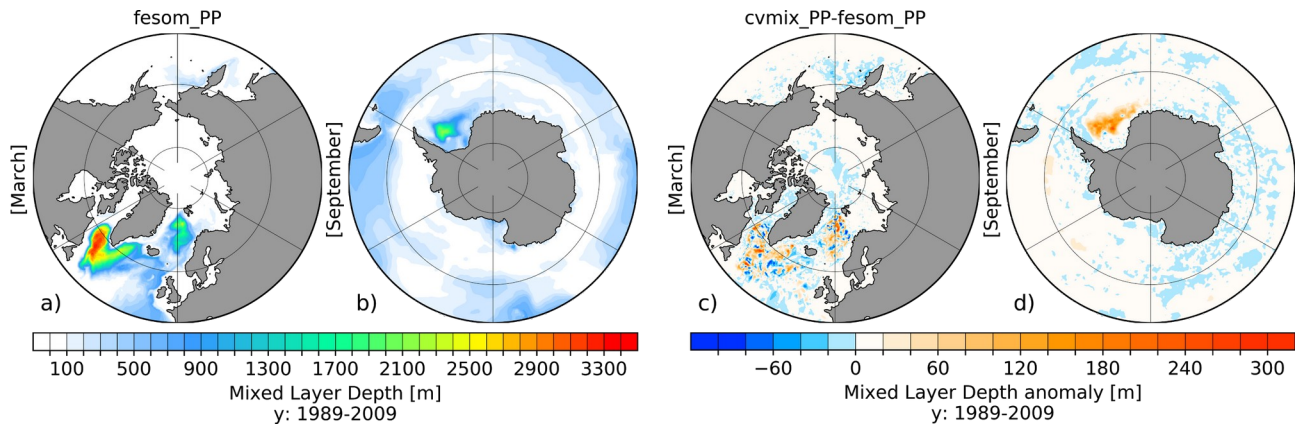
1006 **Figure 10:** Northern hemispheric March (a) and southern Hemispheric September (b) mixed layer depth
 1007 (MLD) for *fesom* ~~original-FESOM2.0~~-KPP implementation as well as corresponding anomalous MLD
 1008 between *cvmix_KPP* and *fesom* ~~CVMIX~~ and original *FESOM2.0*-KPP implementation (c, d), averaged for
 1009 the period 1989-2009.



1010

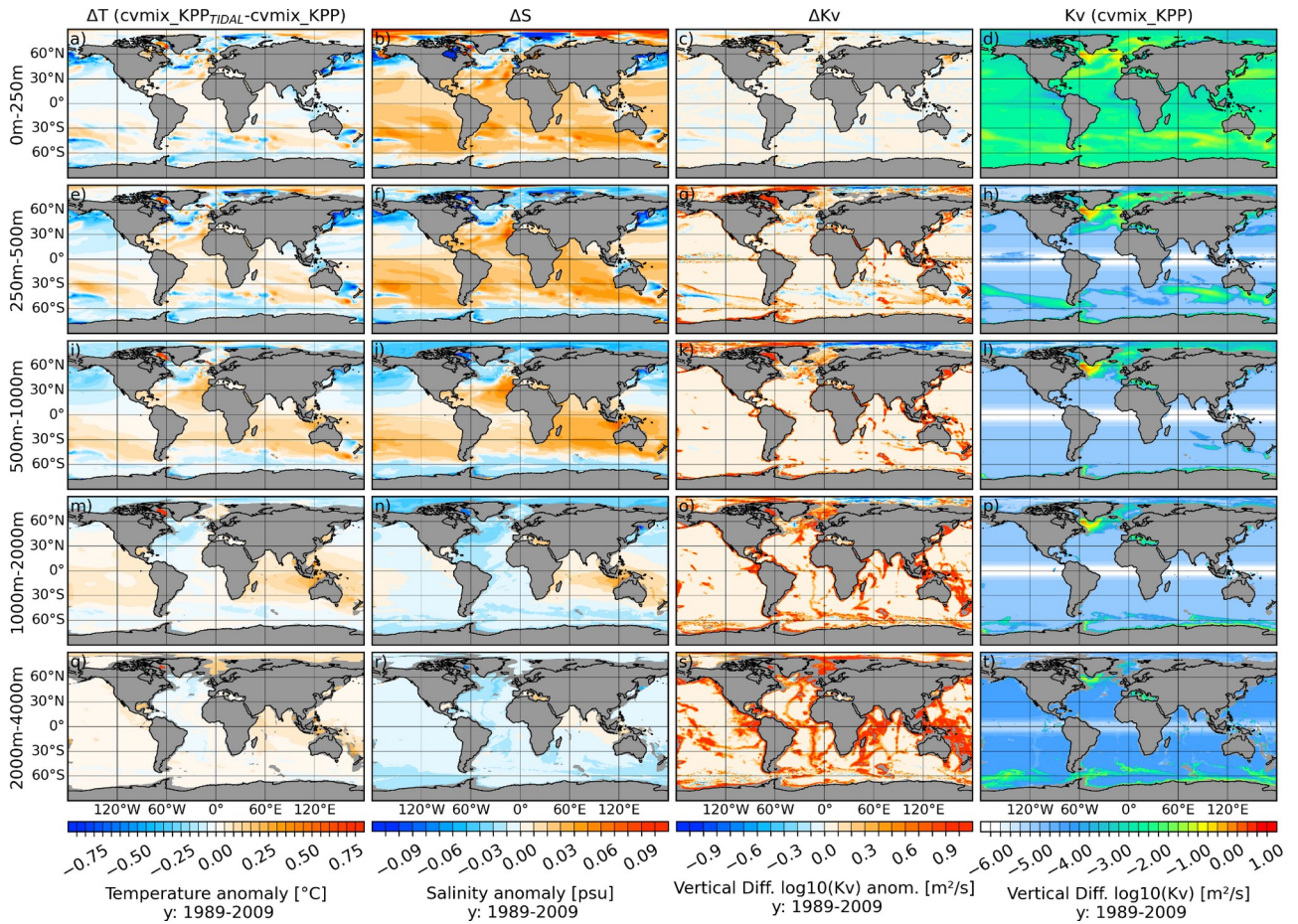
1011 **Figure 11:** Temperature (1st Column), salinity (2nd column) and vertical diffusivity (3rd column) difference
 1012 between `cvmix_PP` and original `fesom_PP` implementation as well as the absolute vertical diffusivity values
 1013 (4th column) for `fesom_PP` averaged for the period 1989 to 2009. From top to bottom, panels show the
 1014 vertically averaged fields for the depth ranges of 0-250 m, 250-500 m, 500-1000 m, 1000-2000 m and 2000-
 1015 4000 m.

1016



1017

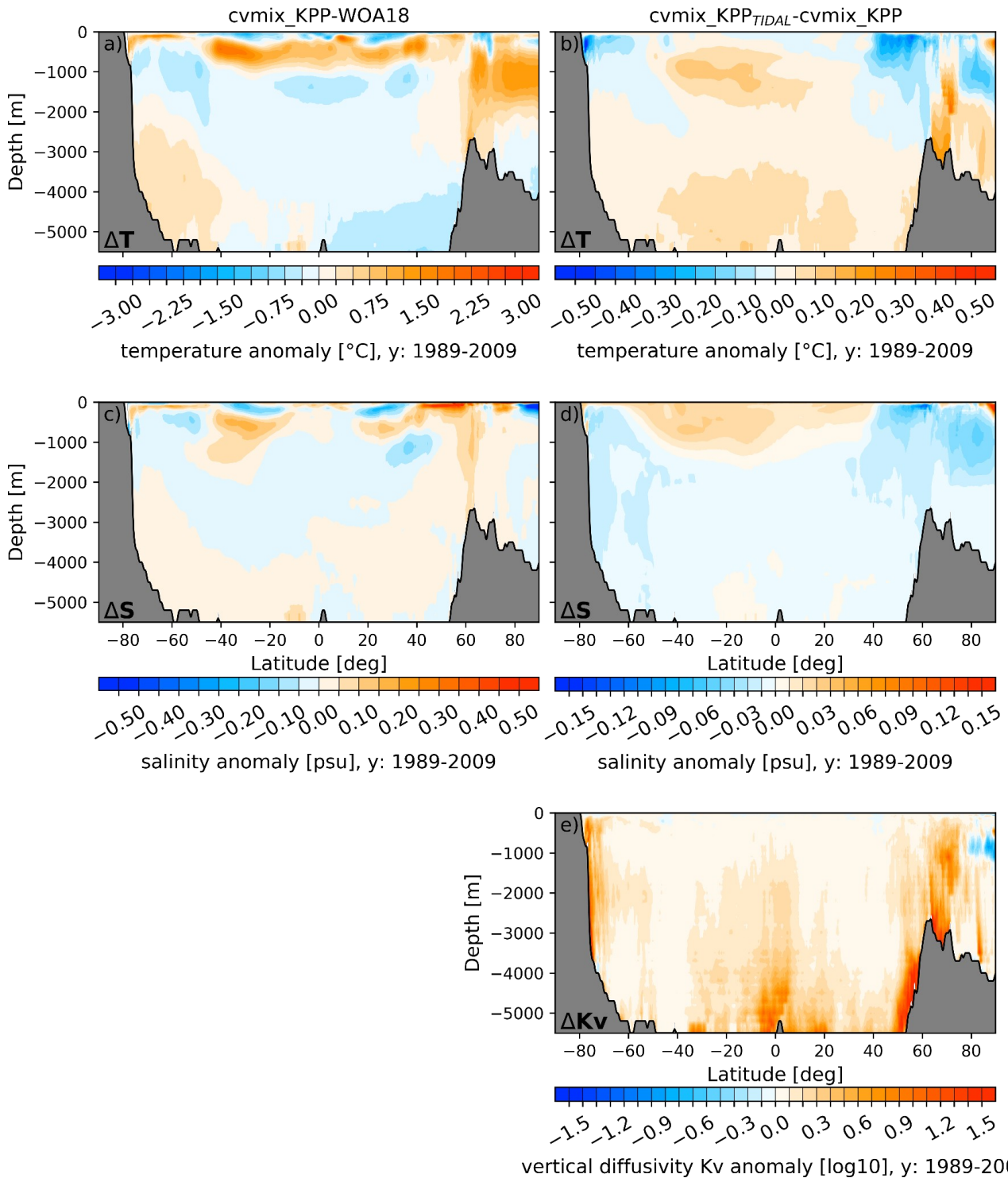
1018 **Figure 12:** Northern hemispheric March (a) and southern Hemispheric September (b) mixed layer depth
 1019 (MLD) for `fesom` original `FESOM2.0-PP` implementation as well as corresponding anomalous MLD
 1020 between `cvmix_PP` and `fesom_CVMIX` and original `FESOM2.0-PP` implementation (c, d), averaged for the
 1021 period 1989-2009.



1022

1023 **Figure 13:** Temperature (1st Column), salinity (2nd column) and vertical diffusivity (3rd column) difference
 1024 between cvmix_KPP_TIDAL and cvmix_KPP with and without TIDAL mixing of Simmons et al. (2004) as well as the
 1025 absolute vertical diffusivity values (4th column) for cvmix_KPP without TIDAL mixing averaged
 1026 for the period 1989 to 2009. From top to bottom, panels show the vertically averaged fields for the depth
 1027 ranges of 0-250 m, 250-500 m, 500-1000 m, 1000-2000 m and 2000-4000 m.

1028



1029

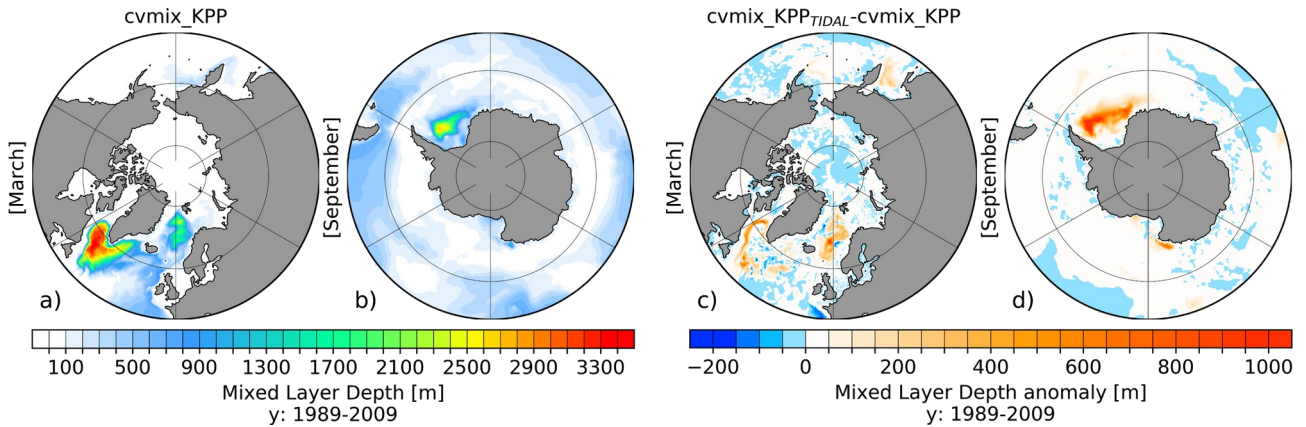
1030 **Figure 14:** Left column: presents global Global-zonal averaged climatological biases of temperature (a) and ;
 1031 b), salinity (c) bias , d) and vertical diffusivity (e) profiles of cvmix_KPP with respect to WOA18. Right
 1032 column: shows the global zonal averaged biases of temperature (b), salinity (d) and vertical diffusivity (e)
 1033 between to WOA18 (a, c) and of cvmix_KPP with tidal mixing of Simmons et al. (2004) versus without (e,
 1034 d, e).

1035

1036

1037

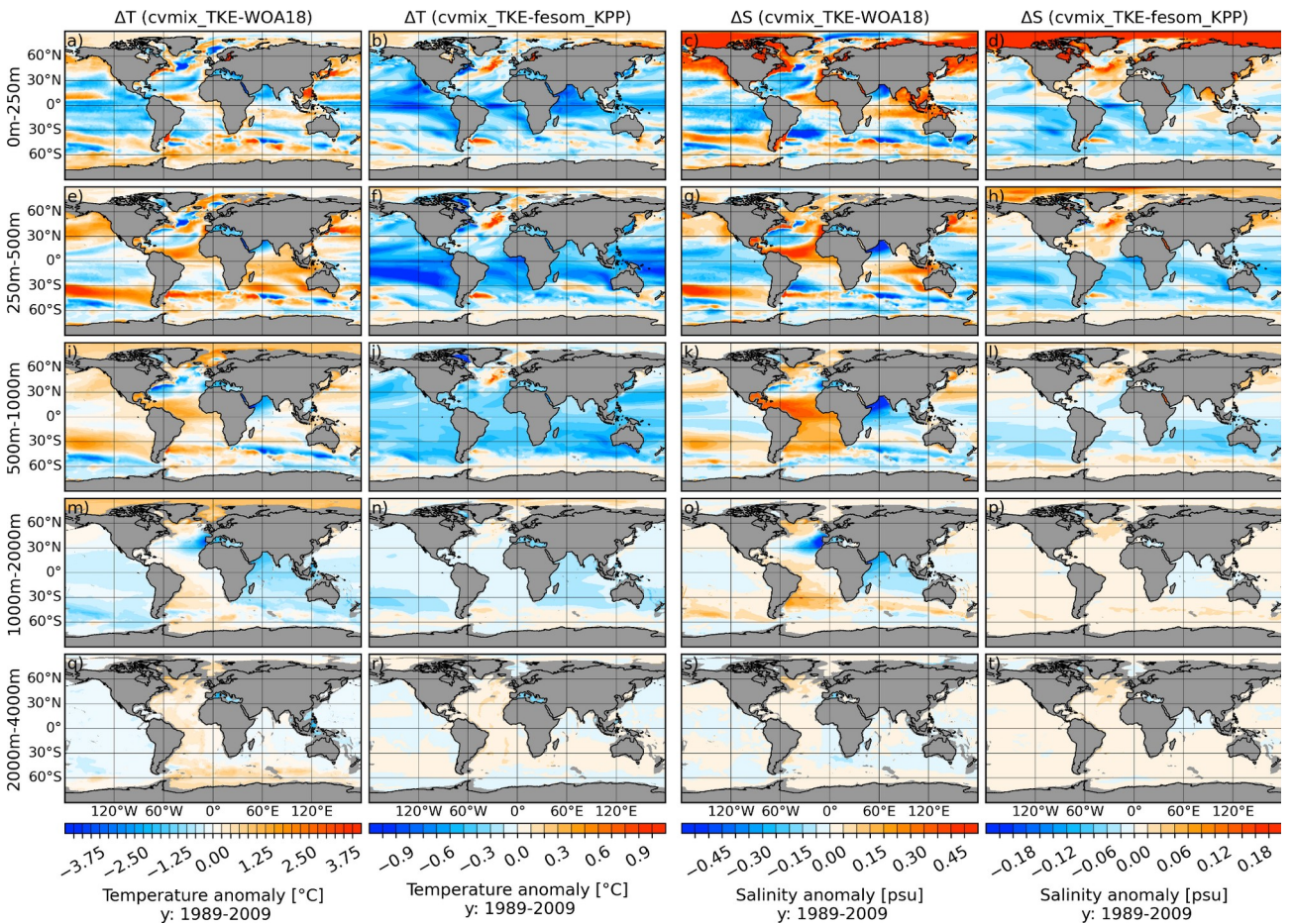
73
1038
1039



1040

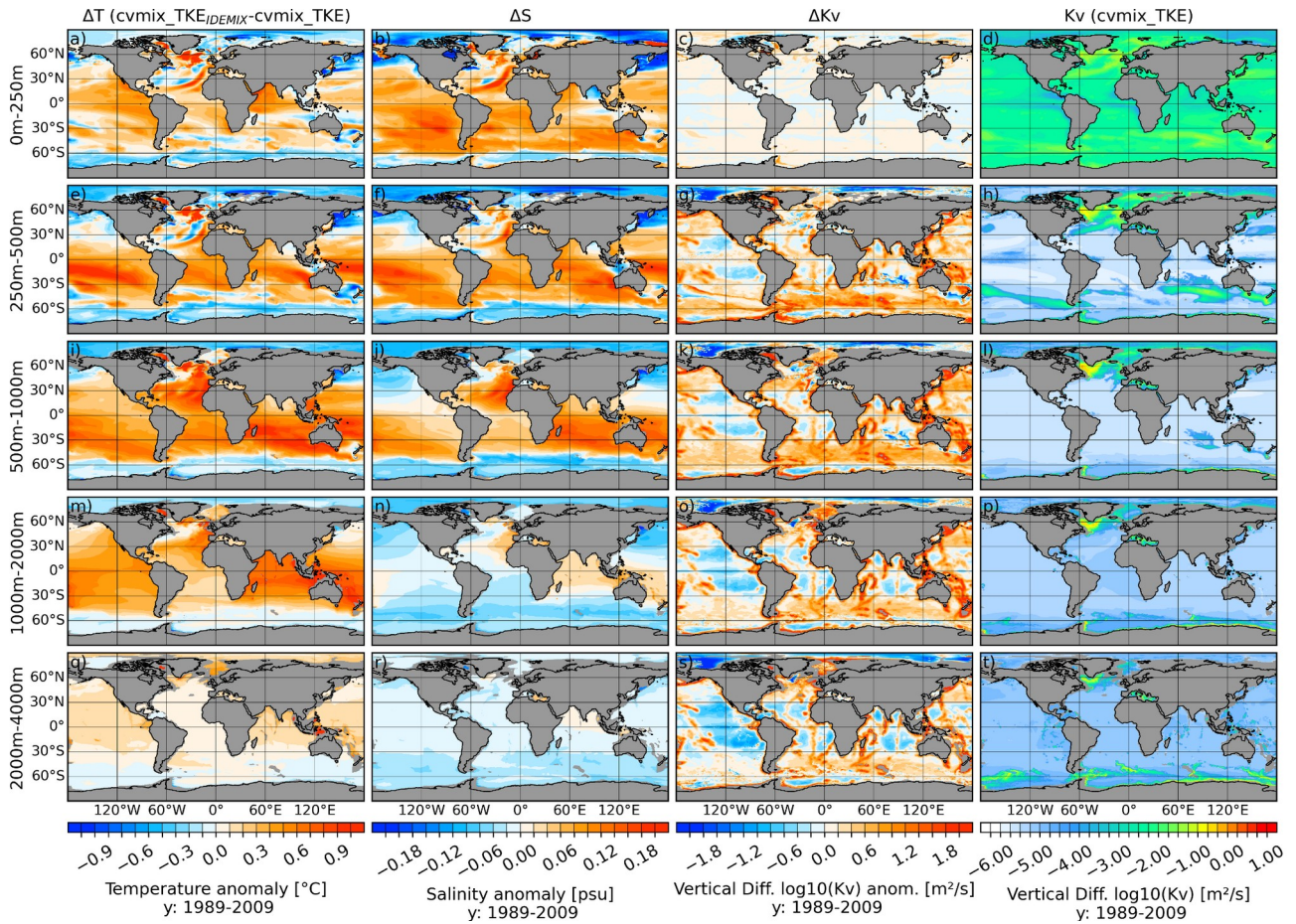
1041 **Figure 15:** Northern hemispheric March (a) and southern Hemispheric September (b) mixed layer depth
1042 (MLD) for cvmix_KPP without TIDAL mixing as well as corresponding anomalous MLD between
1043 cvmix_KPP with minus without TIDAL mixing of Simmons et al. (2004)(c, d), averaged for the period
1044 1989-2009.

1045



1046

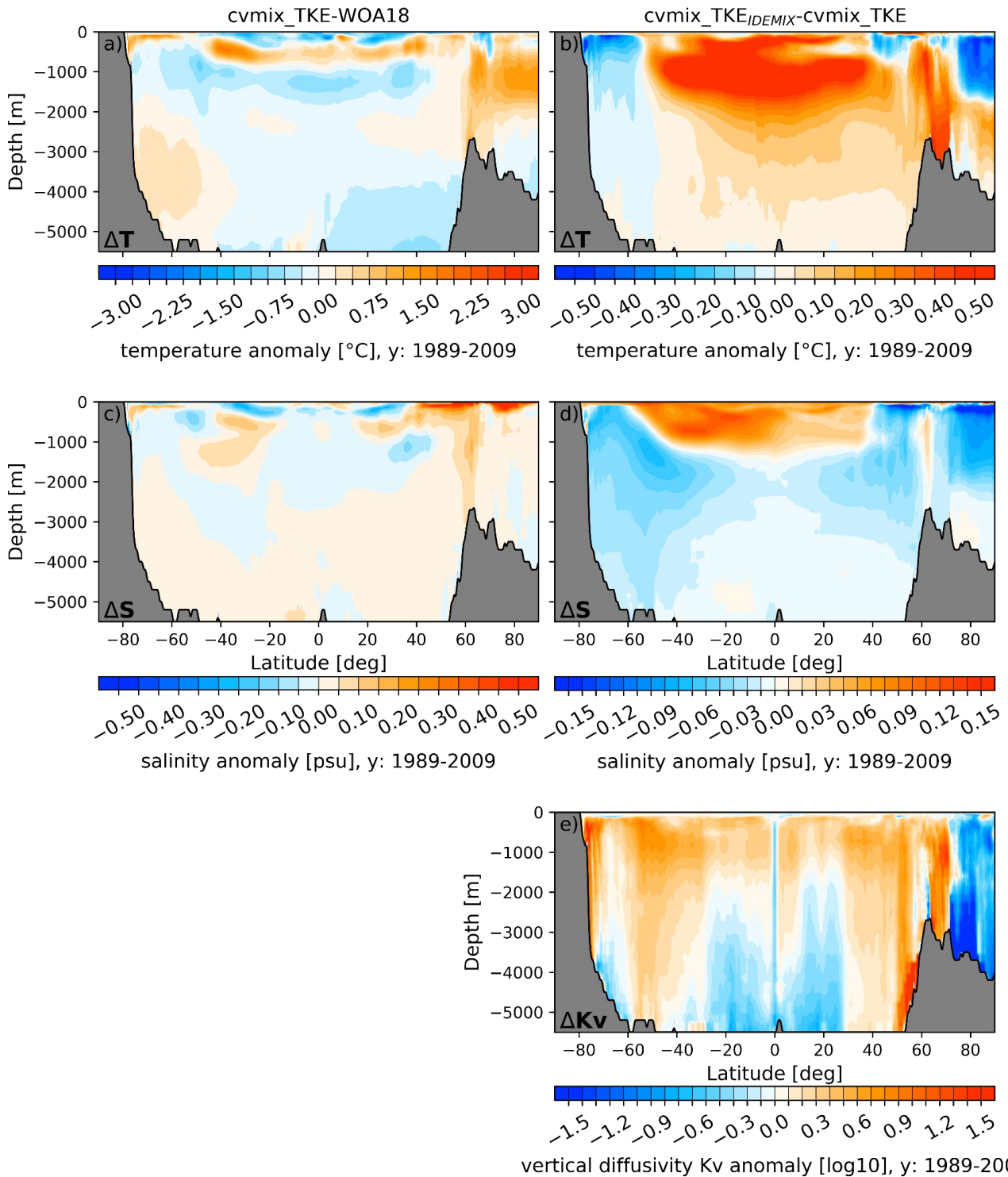
1047 **Figure 16:** Temperature (1st and 2nd column), salinity (3rd and 4th column) difference between cvmix_TKE
1048 and WOA18 (1st and 3rd column) as well as between cvmix_TKE and fesom_KPP (2nd and 4th column)
1049 averaged for the period 1989 to 2009. From top to bottom, panels show the vertically averaged fields for the
1050 depth ranges of 0-250 m, 250-500 m, 500-1000 m, 1000-2000 m and 2000-4000 m.
1051



1052

1053 **Figure 17:** Temperature (1st Column), salinity (2nd column) and vertical diffusivity (3rd column) difference
 1054 between cvmix_TKE with and without IDEMIX as well as the absolute vertical diffusivity values (4th
 1055 column) for cvmix_TKE without IDEMIX mixing averaged for the period 1989 to 2009. From top to
 1056 bottom, panels show the vertically averaged fields for the depth ranges of 0-250 m, 250-500 m, 500-1000 m,
 1057 1000-2000 m and 2000-4000 m.

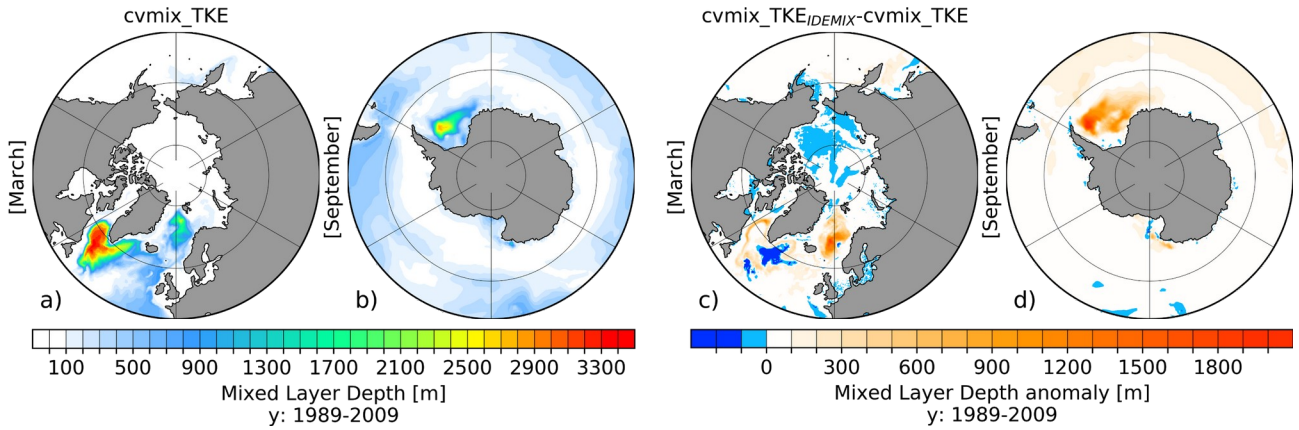
1058



1059

1060 **Figure 18:** Left column: presents global Global-zonal averaged climatological biases of temperature (a) and ;
 1061 b), salinity (c) bias, d) and vertical diffusivity (e) profiles of cvmix_TKE with respect to WOA18. Right
 1062 column: shows the global zonal averaged biases of temperature (b), salinity (d) and vertical diffusivity (e)
 1063 between to WOA18 (a, e) and of cvmix_TKE with IDEMIX versus without (c, d, e).

1064

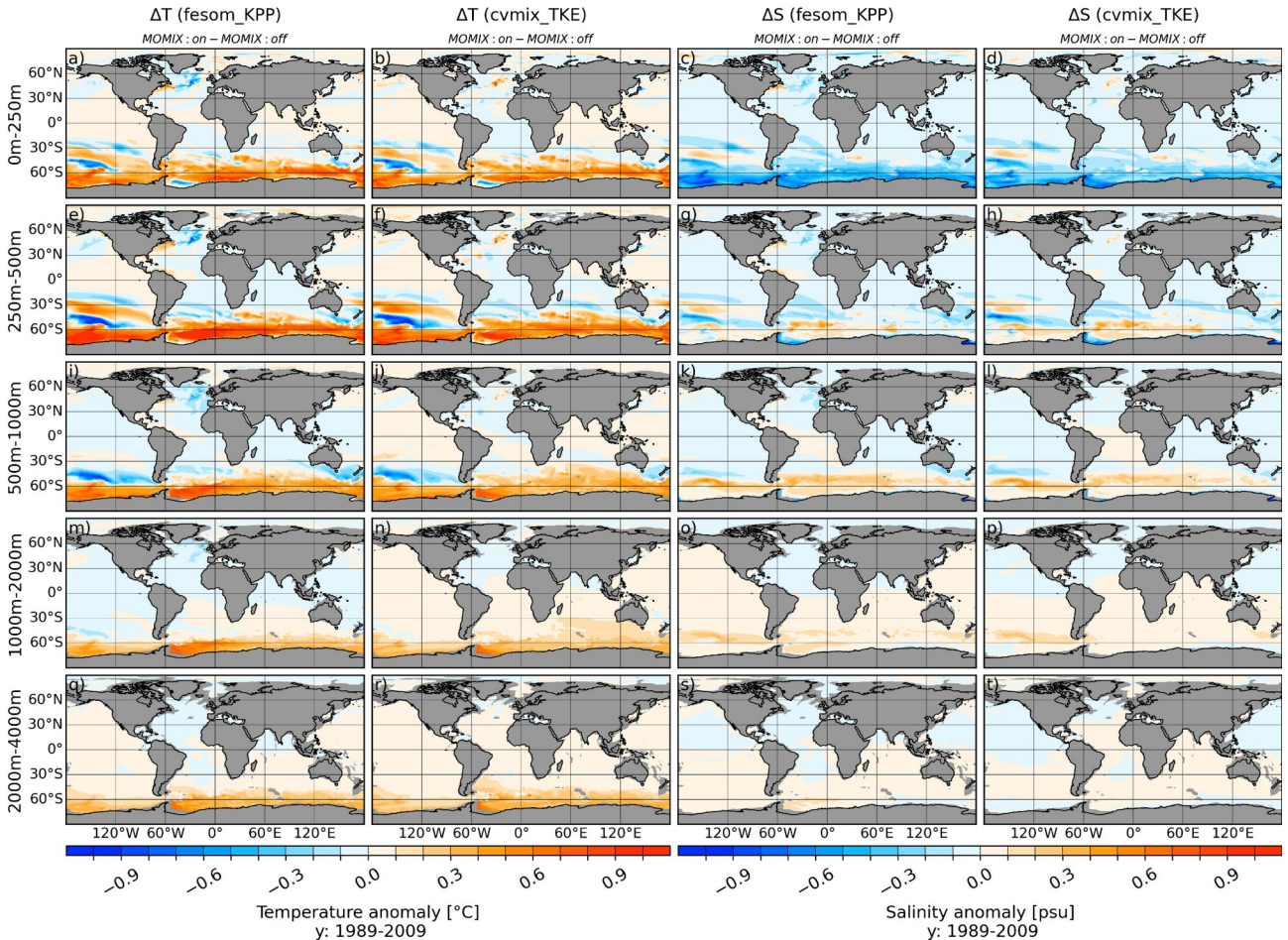


1065

1066 **Figure 19:** Northern hemispheric March (a) and southern Hemispheric September (b) mixed layer depth
 1067 (MLD) for cvmix_TKE without IDEMIX mixing as well as corresponding anomalous MLD between
 1068 cvmix_TKE with minus without IDEMIX mixing, averaged for the period 1989-2009.

1069

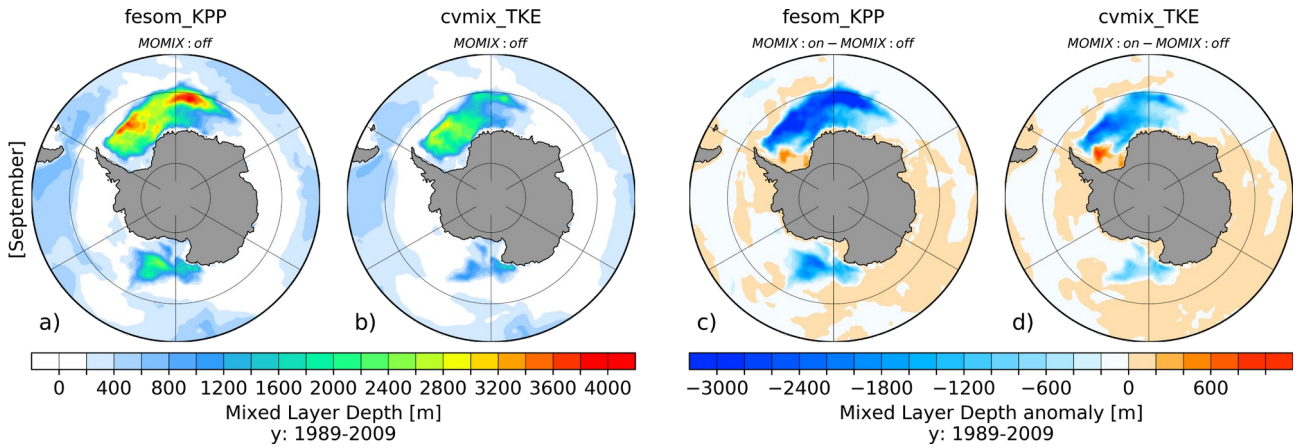
1070



1071

1072 **Figure 20:** Temperature (1st and 2nd column), salinity (3rd and 4th column) difference between fesom_KPP
 1073 and cvmix_TKE vertical mixing parameterisation with Monin-Obukov vertical mixing (MOMIX) switch on
 1074 and off (MOMIX: on minus MOMIX: off) averaged for the period 1989 to 2009. From top to bottom, panels
 1075 show the vertically averaged fields for the depth ranges of 0-250 m, 250-500 m, 500-1000 m, 1000-2000 m
 1076 and 2000-4000 m.

1077

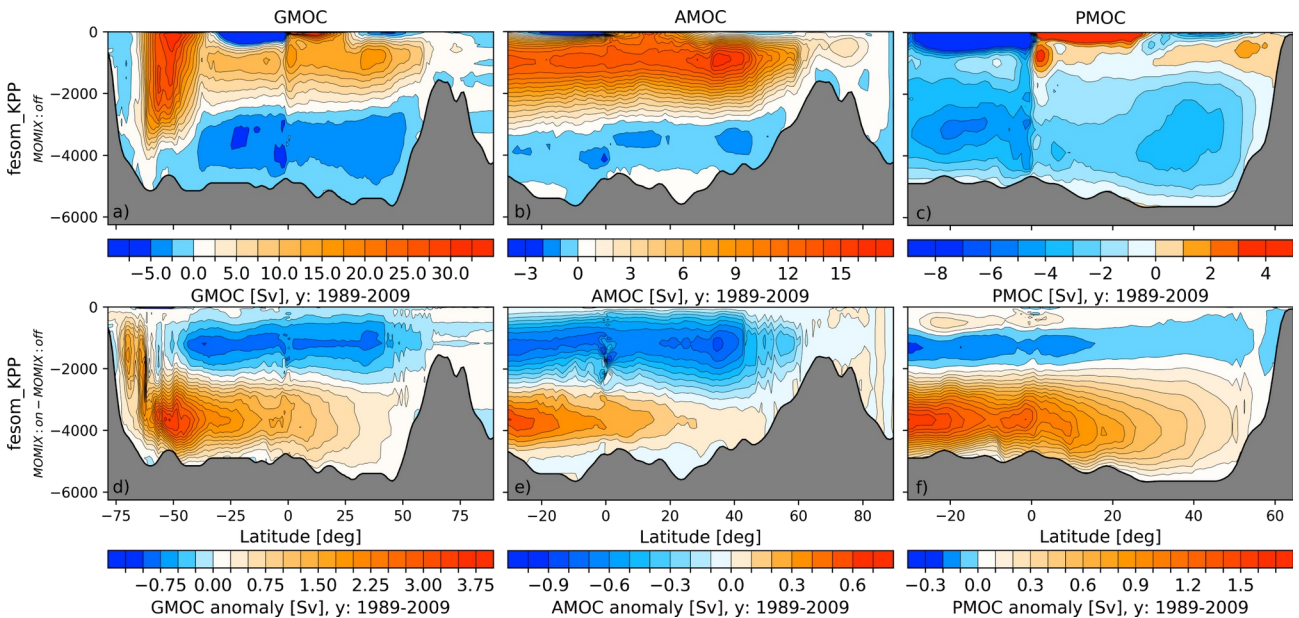


1078

1079 **Figure 21:** Southern Hemispheric September mixed layer depth (MLD) for fesom_KPP (a) and cvmix_TKE
 1080 (b) with switch off Monin-Obukov vertical mixing (MOMIX) parameterisation as well as corresponding
 1081 anomalous MLD between switched on and off MOMIX parameterisation (c, d, MOMIX: on minus MOMIX:
 1082 off), averaged for the period 1989-2009.

1083

1084



1085

1086 **Figure 22:** Absolute (upper row) and anomalous (lower row) Global (GMOC, left column), Atlantic
 1087 (AMOC, middle column) and Indo-Pacific (PMOC, right column) Meridional Overturning Circulation,
 1088 averaged for the time period 1989-2009. Absolute values are shown for fesom_KPP with switched off
 1089 Monin-Obukov vertical mixing (MOMIX) parameterisation, anomalous values show the difference between
 1090 fesom_KPP with switch on/off MOMIX parameterisation MOMIX: on minus MOMIX: off).

1091

1092